Ocean Engineering 306 (2024) 118057

Contents lists available at ScienceDirect

Ocean Engineering

journal homepage: www.elsevier.com/locate/oceaneng

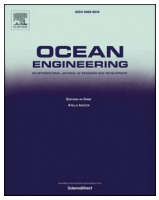

Research paper

Structural analysis of small-scale 3D printed composite tidal turbine blades

Hassan Gonabadi [a,*], Seyed Farhad Hosseini [b], Yao Chen [a], Steve Bull [a]

[a] Newcastle University, School of Engineering, Newcastle Upon Tyne, NE1 7RU, UK
[b] Hamburg University of Technology, Am Schwarzenberg-Campus 4 (C), 21073, Hamburg, Germany

A B S T R A C T

The existing research literature lacks comprehensive investigations into assessing the structural performance of marine renewable energy conversion devices, particularly 3D printed turbine blades, which often rely solely on computational modelling without experimental validation methods and/or established mechanical characterization techniques. This leads to significant uncertainty regarding the performance of 3D printed turbine blades manufactured by additive manufacturing technology. This study aims to fill this gap by proposing a procedure for evaluating the structural integrity of commercial small-scale tidal turbine blade (5 KW) manufactured using fused filament fabrication 3D printing with a linear infill pattern. This is achieved by developing a combined experimental, hydrodynamic, and finite element approach with the view to inspect the micro-mechanical properties of representative volume elements of 3D printed microstructures using homogenization technique. The results of mechanical testing and hydrodynamic modelling are used to create a finite element model of the 3D printed blade, allowing for stress and failure analysis. Findings indicate that while integrating 3D printed materials into blade design via 3D printing technology is feasible, the choice of materials is limited to high stiffness composite filaments. Finally, experimental validation of numerical results, particularly full field strain distribution maps obtained by digital image correlation technique for flexural testing and laboratory-scale 3D printed blade, confirms the accuracy of the finite element results. Finite element-based homogenization techniques provide valuable insights into potential failure modes in 3D printed tidal turbine blades. However, the expedited calculation of orthotropic properties through finite element analysis proves to be a faster mechanical characterization method compared to experimental approaches. The proposed methodology in this study facilitates quicker iterative design of 3D printed blades, thereby reducing the need for repeated experiments and ultimately lowering manufacturing costs.

1. Introduction

Marine energy, emerging as a sustainable power source, has gained significant traction recently. Its environmental friendliness and predictability distinguish tidal systems from other renewables like wind energy. Moreover, due to the higher density of seawater compared to air, tidal generators produce more power with smaller blades, making them efficient in energy delivery.

So far, in the available generators of the tidal energy systems which are being evaluated commercially, horizontal axis turbine blade (HATT) is mainly used. Hydrodynamic forces acting on rotating blades generate both thrust and tangential forces. The thrust force, perpendicular to the blade's surface, propels the blade along its rotational path, while the tangential force, parallel to the surface, induces rotation. Pressure imbalances around the blade caused by seawater motion result in these forces, with the blade's shape and angle influencing their magnitude and direction. Consequently, the combined effect of thrust and tangential forces leads to continuous blade rotation. Seawater has quite high density-ratio which means it can generate higher torque, however, because of the high density of sea water, the bending moment is significant and therefore the induced strain at the blade root is much higher compared to wind turbine blades. As a result, shorter blade designs are usually favourable for tidal turbines.

Although recent investigations on reducing the cost of tidal energy systems via advanced structural materials (Kennedy et al., 2018; Grogan et al., 2013; Gonabadi et al., 2022a; Porter et al., 2020; Murray et al., 2018; Davies et al., 2022; Harper et al., 2015; Glennon et al., 2022; Finnegan et al., 2021) has led to the use of glass or carbon fibre reinforced polymer composites in blade structures with acceptable structural performance and life expectancy, still cost and time of conventional manufacturing processes (e.g. Resin Transfer Moulding) of these load bearing components is high, limiting the number of locations where tidal turbines can be cost-effectively deployed. At present this has limited tidal turbines to high tidal flow sites where the potential energy generation is noteworthy and will cover the capital cost of the system. Although not too many, there are a very large number of sites around the world, with lower tidal flow speeds (between 1 m/s and 2 m/s) which could be used to allow a tidal turbine to be widely deployed if an efficient, cheap, simple and less labour-intensive manufacturing method is available.

* Corresponding author.
E-mail address: Hassan.gonabadi57@gmail.com (H. Gonabadi).

https://doi.org/10.1016/j.oceaneng.2024.118057
Received 9 March 2024; Received in revised form 28 April 2024; Accepted 28 April 2024
Available online 4 May 2024

As the 3D printing technology has become more mature, it is now viable to use the 3D printing method to manufacture tidal turbine blades. 3D printers use layer by layer deposition of semi-molten materials to make complex shapes according to the computer aided design (Gonabadi et al., 2020; Chadha et al., 2019; Tang et al., 2020; Kamaal et al., 2021; Naveed, 2021). This method significantly improves the flexibility of the design resulting in high precision of a complex blade design compared to conventional manufacture. Besides, due to its integrated manufacturing method, the 3D-printing reduces the time of assembling each part of the blade by adhesives. And it also saves the time of curing the blade made from thermosetting resins which is necessary to withstand the high operating stresses.

In recent years, computer-aided engineering (CAE) methods have been employed to assess the structural integrity of small-scale 3D printed wind/marine turbine blades. However, there has been few studies focusing on fully characterizing the mechanical properties of these printed structures and validating finite element (FE) results, leaving the reliability of numerical predictions and performance of 3D printed blades uncertain. Malim, A. et al. in an investigation developed a new method for designing and analysing 3D-printed propeller blades for high-altitude UAVs, utilizing a macroscale numerical model validated through experimental testing. This approach demonstrates accurate prediction of deformation and stress levels, affirming the feasibility of 3D printing full-scale propeller blades for such applications (Malim et al., 2023). While some studies (Kim et al., 2018; Galvez et al., 2022; Arivalagan et al., 2023; Rouway et al., 2021; Kim, 2017) have also explored additive manufacturing for horizontal axis turbine blades, the impact of 3D printed microstructures on tidal turbine blade design has not been fully investigated. Experimental determination of the real orthotropic mechanical properties of 3D printed lattice structures and validation of FE-induced strains and tip deflection on the blade remain unexplored areas.

In the present investigation, the first challenge of determining the real mechanical properties of 3D printed cellular lattice structure which are to be fed into the FE model of 3D printed blade is addressed by performing standard mechanical tests on 3D printed tension and shear specimens. This has been accompanied by numerical micromechanics of representative volume element (RVE) using FE homogenization method, therefore, effective orthotropic properties of RVE have been determined by FE computational methods as well. In previous studies (Park et al., 2014; Liu et al., 2016; Guessasma, 2008; Tucker et al., 1999; Sun et al., 1996; Gonabadi et al., 2021a, 2022b), it has been shown that the FE predicted elastic response of 3D printed parts using homogenization technique is experimentally validated, therefore, the mechanical properties of RVE can be calculated by conducting standard tensile and shear tests. In this work, homogenized continuum FE modelling of blade, instead of FE microstructural modelling, generates less elements, and therefore reducing the computational time. This has been proved through the verification of FE results against the experiments in section 3.2.1 and section 4 of this work.

The present study, establishes a design procedure for the initial evaluation of the structural integrity of small-scale 3D printed turbine blades using different 3D printed materials with the objective of addressing the knowledge gap of using additive manufacturing technology to produce tidal turbine blades. This is done by developing a combined experimental, hydrodynamic and FE computational methodology with the view to examine the micro-mechanical properties of 3D printed cellular lattice structures when linear infill pattern is used. The methodology incorporates: (a) tensile and shear testing of 3D printed specimens to determine mechanical properties of RVE; (b) a hydrodynamic model-blade element momentum (BEM) theory to calculate the axial and tangential forces acting on the blade; (c) FE structural analysis of the 3D printed blade. Finally, the results of finite element are validated against the experimental data through the FE and digital image correlation (DIC) computed strain distribution maps on a laboratory-scale 3D printed blade. The tidal turbine blade design methodology presented here would enable engineers and manufacturers in tidal energy sectors to design and manufacture printable blades based on the selection of appropriate raw materials (filaments) and optimization of the 3D printed blade model in order to generate a cost-effective blade with suitable mechanical properties for low tidal speed services.

2. Methodology

2.1. Sample preparation and mechanical characterization

The proposed work of this study to design and manufacture small scale tidal turbine blades using 3D printing technology (i.e. fused filament fabrication of 3D printing process) is based on the use of 3D printed cellular lattice structure of RVE with the linear infill pattern, therefore the first stage of this study is to fully characterize the mechanical behaviour of RVE made up of three candidate materials (i.e. 30% short glass fibre reinforced polyamide (SGF/PA), 15% short carbon fibre reinforced polyamide (SCF/PA) and polylactic acid known as PLA). These are important information that need to be fed into the FE model of 3D printed small scale blade to parameterize the numerical simulation. In this study, standard testing methods of ASTM D638, ASTM D5379 and ASTM D2344 (Committee, 2008; ASTM, 2012; Materials, 2006), were used to manufacture tensile, Iosipescu shear and short beam shear test specimens respectively via an Ultimaker 3 3D printing device. Using the same ASTM standard testing methods described above, the mechanical testing of tension and shear were conducted. Tensile and shear tests were conducted on 3D-printed specimens using a Tinius Olsen Universal testing machine equipped with a 50 kN load cell, offering an accuracy of ±0.5%. The key point in the present study is the use of Digital Image Correlation (DIC) technique during the above mechanical testing, which facilitated the measurement of strain and Poisson ratio values, therefore, the stress-strain curves were constructed and components of elastic moduli and strength parameters were determined. Apart from the PLA material which its mechanical properties have been fully investigated in previous works (Gonabadi et al., 2020, 2022b), SGF/PA and SCF/PA composite filaments (2.85 mm/500 g) and (2.85 mm/750 g) respectively were used to fabricate the 3D printed samples. The parameters used in 3D printing machine to fabricate the above tensile and shear test samples are shown in Table 1. Fig. 1 schematically shows a typical 3D FFF printer, where the 3D printed components are made in a layer-by-layer manner.

To determine the orthotropic engineering constants of RVEs of 3D printed blade, tensile, Iosipescu and short beam shear (SBS) test samples were initially printed with various raster and build orientations using parallel deposited filaments, finally, mechanical testing of tensile, Iosipescu and short beam shear tests were carried out in combination with DIC system (Kim, 2017) to map the strain fields, to build the stress-strain curves and to extract the elastic constants. The infill patterns and printing orientation of 3D printed samples are shown in Fig. 2. In previous investigation (Gonabadi et al., 2022b), it has been shown that conducting (1) tensile tests on 3D printed specimens with raster angle of 0 °, 90 ° and build orientation of upright, (2) Iosipescu shear tests on 3D printed samples with raster angle of 0 ° and build orientation of upright and (3) SBS test on 3D printed sample with the 90 ° raster angle, will

Table 1
Parameters used in 3D printing machine to fabricate the test samples.

Printing parameter	value
Temperature of extruder (°C)	250
Extrusion multiplier (%)	100
Deposition velocity (mm/s)	60
Temperature of bed (°C)	110
Diameter of nozzle (mm)	0.4
Layer height (mm)	0.2
Overlap (%)	10
Build platform material	Glass platform

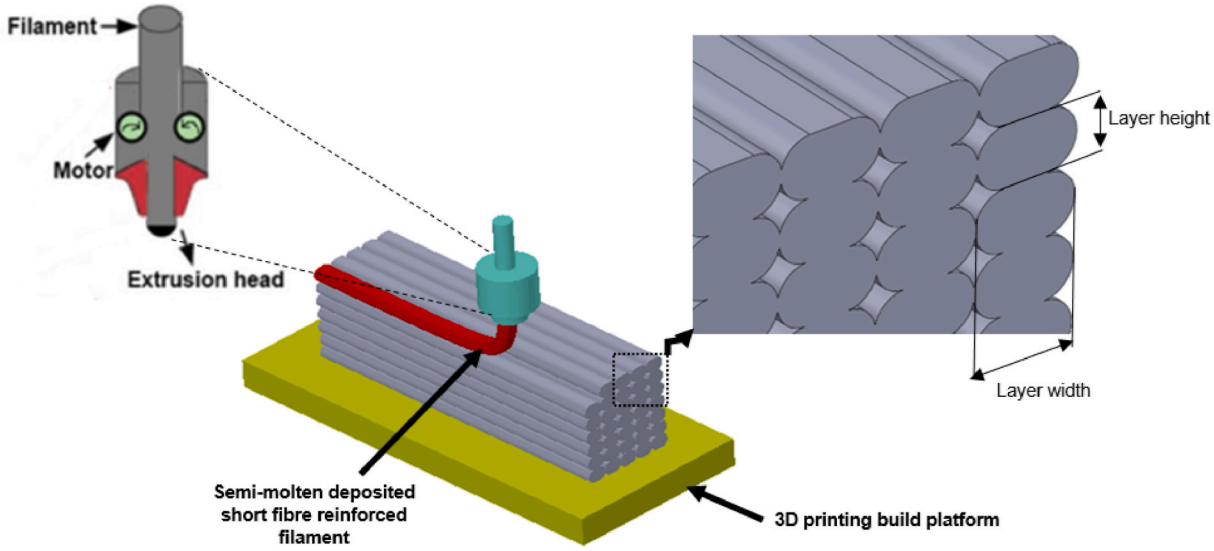

Fig. 1. Schematic representation of fused filament fabrication 3D printer.

result in orthotropic engineering constants of RVE (Table 2).

It must be noted as proved in previous study (Gonabadi et al., 2022b), the components of major and minor Poisson's ratios can be calculated by conducting tensile tests in conjunction with DIC full field strain maps employing virtual extensometers in longitudinal and transverse directions. In the present study, to measure ν_{13} and ν_{12}, DIC full field strain maps were employed on the top side of 3D printed tensile samples with raster angle of 0 ° and build orientation of upright respectively. To measure ν_{23}, the same tensile testing of 3D printed sample with raster angle of 90 ° was conducted, but the DIC full filed strain map was employed on the edge side of this sample, resulting in the calculation of strain in longitudinal and transverse directions, finally the component of Poisson ratio (ν_{23}) was calculated.

2.1.1. Digital image correlation

Full-field deformation measurements were conducted employing the Digital Image Correlation (DIC) technique, which relies on comparing images captured before and after deformation. Image acquisition utilized a CCD camera, with the images subsequently digitized and analysed to generate strain maps. Prior to measurement, specimens were coated alternately with black and white paint to establish a speckle pattern with adequate greyscale contrast for analysis. The camera featured a spatial resolution of 5.5 μm/pixel and was equipped with lenses providing 0.193 magnification at a working distance of approximately 300 mm. An external light source ensured uniform illumination of the entire sample to minimize errors attributable to varying lighting conditions, a crucial aspect for accurate strain mapping. Image acquisition was synchronized with the onset of each mechanical test. DIC enabled comprehensive strain measurement across the surface using the speckle pattern distribution. Images were captured during the tensile test utilizing Imetrum video-gauge software at a rate of 5 Hz, and subsequent processing was carried out using VIC-2D software from Correlated Solutions, Inc. This software facilitated point interpolation and provided full-field strain maps and stress-strain curves for the 3D-printed specimen. In this study, the accuracy of DIC strain measurements was around 5% below 0.4% strain, with higher accuracies near 2% above 3% strain and 7% for the strain values between 0.4% and 3%.

2.2. Micro-mechanic analysis of RVE based on FE homogenization method

In addition to determining the mechanical properties of an RVE using an experimental approach, micro-mechanical analysis of RVE models is conducted to calculate effective orthotropic properties via FE homogenization technique (Gonabadi et al., 2021a, 2022b). This is done to show that FE-computed elastic properties of RVE micro-structures match with engineering constants obtained through tensile and shear tests. Fig. 3 shows a diagram of the multi-scale FE-homogenization method. The micro length scale model of the RVE is linked with the macro length scale model of a turbine blade through a meso-scale model of an RVE unit cell. The mechanical properties of the elements, i.e., reinforcing fibres and the polymer matrix, and their configuration in the 3D printed filaments control the macro mechanical performance of 3D printed parts; therefore, the orthotropic mechanical properties of a component made up of 3D printed filaments can be estimated by using the FE-homogenization technique as detailed schematically in Fig. 3. In order to determine the elastic constants of the RVE, an FE-based homogenization methodology is used via the material designer module of the FE program (ANSYS). The RVE of the 3D printed composite consists of a filament region with a repetitive pattern. The filament material is actually made up of elements of reinforcing fibre and polymeric matrix at the micro-scale level. As a result, the effective orthotropic properties of the filament can be predicted from the mechanical properties of reinforcing fibre and the polymeric matrix using the cellular lattice structure (unit cell) shown in Fig. 3(a) where individual fibres are randomly distributed with greater dominance in the longitudinal direction of the filament. FE homogenization of the elastic properties of the filament and the inclusion of its architecture result in the effective orthotropic engineering constants of the RVE at the meso-scale level. Therefore, FE analysis of the RVE at the micro-scale level (Fig. 3(a)) using the homogenization technique was initially carried out. The mechanical properties of composite constituents (i.e., glass fibre, carbon fibres, and polyamide matrix) as well as the physical features of fibres used in the FE model are shown in Table 3 and Table 4 respectively. The micro-model of the RVE shown in Fig. 3(a) is then subjected to six different states of tensile and shear strains using specific periodic boundary conditions (PBC) (Gonabadi et al., 2021a, 2022b). This generates the effective orthotropic properties of the micro-scale model of the RVE, which are consequently used as the input properties into the meso-scale RVE in Fig. 3(b). The meso-scale model of the RVE is again subjected to the six different states of tensile and shear strains described earlier given the PBC, resulting in the effective orthotropic properties that are needed for the macro-scale model of the tidal turbine blade. It must be noted that the profile of deposited filaments with a rounded rectangular cross-section and the overlapping area examined under the optical microscope (Fig. 4) were used to measure the layer height and

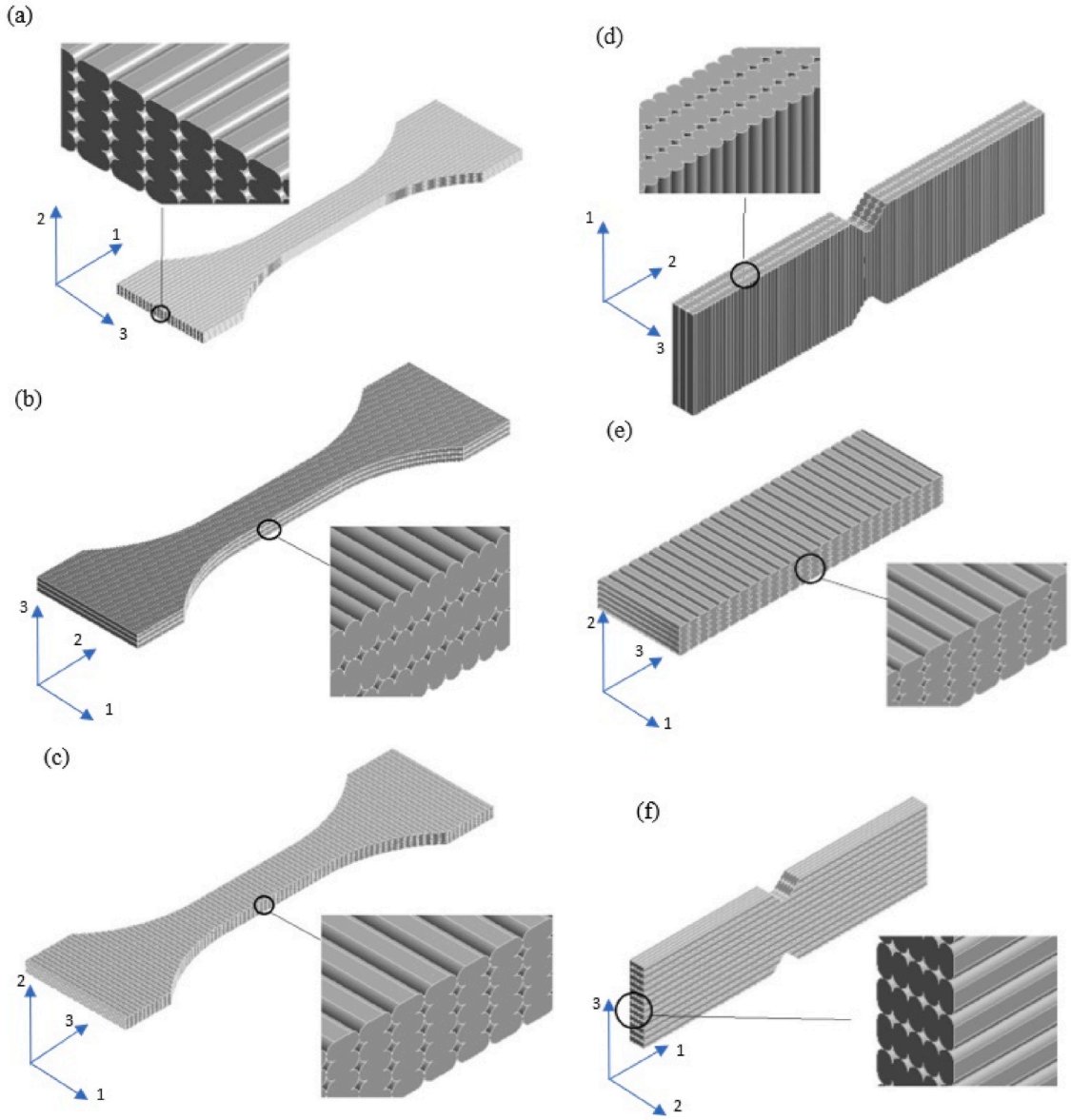

Fig. 2. Schematic representation of 3D printed tensile, Iosipescu and SBS test specimens with the linear infill pattern printed at different raster angle and build orientation. 3D printed tensile test specimens with (a) raster angle of 0 °, (b) build orientation of upright. (c) raster angle of 90 ° (d), 3D printed Iosipescu shear test specimen with the build orientation of upright, (e) 3D printed SBS test specimen with raster angle of 90 ° and (f) 3D printed Iosipescu shear test specimen with raster angle of 0 °.

layer width of the deposited filament; as a result, a more accurate geometry for the FE model of the meso-scale RVE was reconstructed and used in Fig. 3(b) for the present study.

2.3. Combined BEM and FEM

The combined BEM/FEM methodology with mechanical characterization of RVEs via both experimental and numerical techniques was conducted to assess the structural integrity of 3D printed small-scale tidal turbine blades. This was done by conducting an iteration procedure between the failure index (i.e., Tsai-Hill criterion) and mechanical properties of the material (i.e., type of 3D printed filaments) to design a 3D printed blade. In this study, the external geometry of the blade (distributions of radial chord length and twist angle) was determined using a hydrodynamic model based on BEM theory. Additionally, the axial and tangential loads acting on the blade as a result from tidal currents were determined using the same approach in BEM. These axial and tangential forces calculated by BEMT were used as boundary conditions and applied to the FE model of the small-scale 3D printed blade; therefore, FE stress/strain analysis on the 3D printed model of the blade was conducted, resulting in identifying the hot spots on the blade. Constituents of FE-induced stresses/strains at the hot spots of the blade with reference to the maximum allowable tensile and shear strength of RVEs were considered as the Tsai-Hill failure criterion for choosing 3D printed filaments.

2.3.1. BEMT methodology

The hydrodynamic model based on BEM theory, which was developed in the previous study (Gonabadi et al., 2022a) was used to optimize the blade shape and provide boundary conditions for the FE structural analysis of 3D printed blades. To design the blade shape using a hydrofoil type of NACA 4415 and predict the fluid-blade force distribution, a MATLAB code based on a BEM model was used. The full explanation of the equations used in the BEMT code has been provided in (Kennedy

Table 2
Mechanical testing methods and the orientation of 3D printed tensile, iosipescu and short beam shear test specimens shown in Fig. 2 in order to experimentally determine the elements of moduli.

3D printing orientation (raster angle and build orientation)	Mechanical testing method	Components of elastic modulus
3D printed test specimen with raster angle of 0 °	Tension	E_1
3D printed test specimen with build orientation of upright	Tension	E_2
3D printed test specimen with raster angle of 90 °	Tension	E_3
3D printed shear test specimen with the build orientation of upright	Iosipescue	G_{12}
3D printed SBS shear test specimen with raster angle of 90 °	SBS	G_{23}
3D printed Iosipescu shear test specimen with raster angle of 0 °	Iosipescu	G_{13}
3D printed test specimen with raster angle of 0 ° using the DIC full field strain measurement of the top side of tensile sample	Tension	ν_{13}
3D printed test specimen with build orientation of upright using the DIC full field strain measurement of the top side of tensile sample	Tension	ν_{12}
3D printed test specimen with raster angle of 90 ° using the DIC full field strain measurement of the edge side of tensile sample	Tension	ν_{23}

et al., 2018; Grogan et al., 2013). To provide the input conditions for the BEM analysis, in the present study, a tidal turbine with a blade length of one (1) meter, which has a power output of 5 KW at the reference tidal current speed of 2 m/s, was used. In order to determine the optimized rotational velocity, the BEM model was also employed to monitor the change in hydrodynamic efficiency with respect to the speed ratio of the blade tip. Therefore, the maximum hydrodynamic efficiency based on the Betz limit was attained, and the peak power of 5 KW was obtained at about 60 RPM for this design of the tidal turbine. The input conditions for the BEM model are listed in Table 5. In this study, grid sensitivity analysis was conducted to determine the spanwise number of elements along the blade length, and the flap-wise bending moment was found to converge with 10 spanwise elements (Fig. 5).

2.3.2. FE methodology

The Finite Element model characterizes the blade design using the mechanical properties of the RVE determined from mechanical tests and incorporates the blade profile as well as hydrodynamic loadings calculated from the BEM model. In the first step of the finite element analysis of the 3D printed blade, a computer-aided design tool is employed to generate a three-dimensional shell model of the blade. This model, which combines the distribution of chord length/twist angle with the hydrofoil from the NACA aerofoil, is then imported into the ANSYS Composite Processor (ACP) plugin in the FE software ANSYS (Release, 2012) where orthotropic engineering properties of the RVE of the 3D printed cellular lattice structure, infill pattern, orientation of filaments, and stacking sequences are all defined. Finally, the blade model is transferred into the module of static structural in the FE program of ANSYS to define the boundary conditions. To do this, the remote force function in ANSYS is used to apply the hydrodynamic thrust and tangential loads to the reference points on the external geometry of the FE model of the blade, where the reference points are positioned at 1⁄4 of the chord length backward from the leading edge for each blade section (Spera, 1994). A cantilever beam is considered for the FE model of the blade, so the blade root is constrained in all degrees of freedom. A linear shell element (shell 181) is assigned in the FE model of the blade (ANSYS et al., 2009) and the blade profile (NACA aerofoil) is divided into upper and lower skins, each section including spar caps structures, trailing edge, and leading edge. The lay-up configuration of the linear pattern (0°) of the 3D printed materials is used for each of the above sections; therefore, the ply orientation is at 0° to the blade axis. The shear webs are also introduced between the top and bottom blade skin with the same lay-up configuration of the linear pattern. The spar web cross-section of the blade and infill pattern of the 3D printed lattice structure used in aerofoil sections are shown in Fig. 6 and Table 6. The shear webs run between 0.1 m and 0.8 distances from the root. A mesh sensitivity study is also carried out on the FE model of the blade by

Table 3
Mechanical properties of composite constituents used in FE homogenization process.

Constituents	Properties
Glass fibres	$E_1 = 72$ GPa, $\nu_{12} = 0.22$
Carbon fibres	$E_1 = 225$ GPa, $E_2 = 15$ GPa, $\nu_{12} = 0.2$, $G_{12} = 15$ GPa
Polyamide matrix	$E_1 = 3.5$ GPa, $\nu_{12} = 0.35$

Table 4
Physical features of fibres used in FE model of micro-scale RVE for homogenization analysis.

		Fibre volume fraction	Orientation tensor	Aspect ratio	Fibre dimeter
Micro-scale RVE	SGF/PA	30%	$a_{zz} = 0.7$ $a_{xx} = a_{yy} = 0.15$	10	5 μm
	SCF/PA	15%			

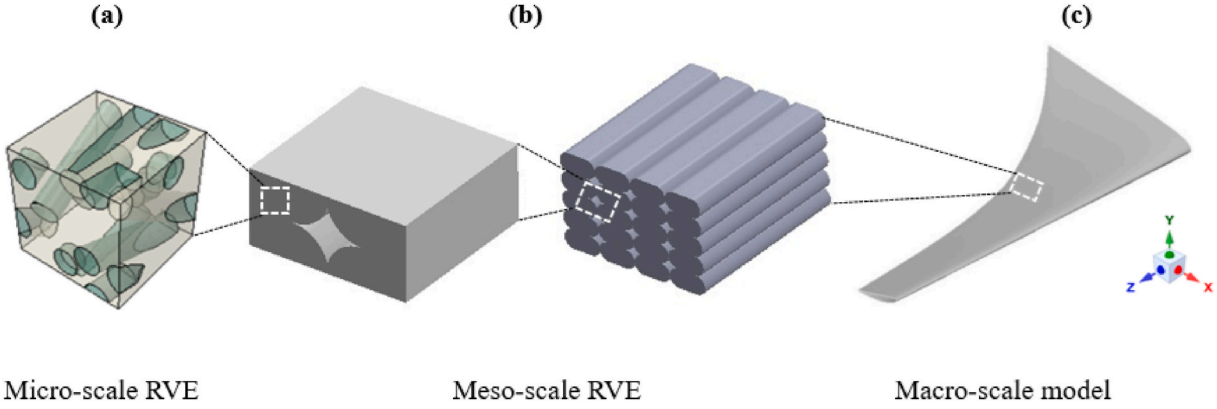

Fig. 3. Diagram of multi-scale FE homogenization analysis implemented to calculate the RVE properties of 3D printed composites. (a) micro-scale of RVE, (b) RVE at meso-scale level and (c) macro-scale model of tidal turbine blade.

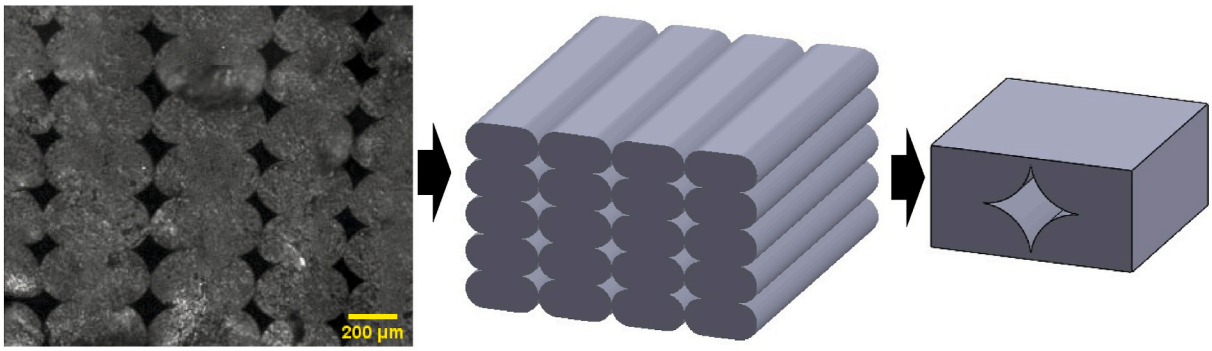

Fig. 4. Micromechanical modelling and re-constructing the meso-scale RVE based on the micrograph of a cross sectional area of 3D printed part showing the geometric size of deposited filaments.

Table 5
Parameters defined for the BEM model at the tidal current speed of 2 m/s.

Parameter	Value
Water velocity	2 (m/s)
Angle of attack	6°
Number of blades	3
Rotation per minute	60
Density of sea water	1025 kg/m3
Seawater viscosity	0.0013155 Pas
Blade length	1 m
Number of blade elements	10

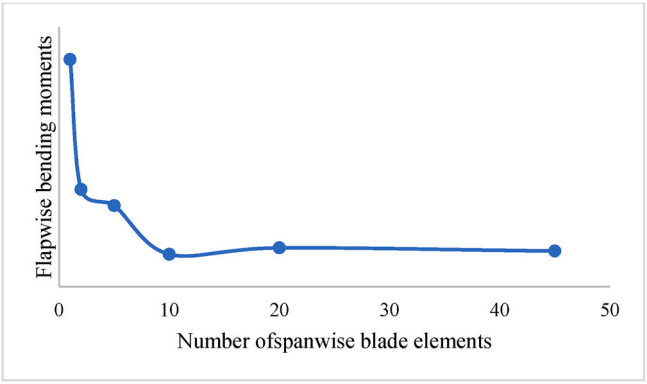

Fig. 5. Grid sensitivity analysis to determine the number of spanwise blade element at the reference seawater velocity of 2 m/s.

refining the density of mesh to ensure that the results of the finite element are mesh-independent (Fig. 7).

2.4. FE structural analysis

For the FE failure analysis of the 3D printed blade, among different failure criteria, the Tsai-Hill failure criterion was employed in this study, as it can reflect the interaction between the components of stresses, therefore, given the anisotropic nature of RVE of 3D printed materials, it is more conservative criterion compared to the other failure theory such as Maximum Strain or Maximum Stress. In the FE model of 3D printed tidal turbine blade, the inverse of the Tsai-Hill index is also calculated for each element as a factor of safety. This factor indicates the strength of the blade design, meaning a high likelihood of blade failure if the safety factor is less than one. To assess the structural behaviour of the 3D printed blade, initially BEM code is executed in order to determine the optimized external blade geometry as well as tangential and thrust force distribution along the blade length. As a result, maximum bending

Table 6
Lay-up configuration of different segments of 3D printed blades.

Aerofoil segments	Infill pattern	Schematic of infill pattern showing the orientation of filaments along the blade length (z axis)
Leading edge Trailing edge Shear webs Spar caps	Linear	

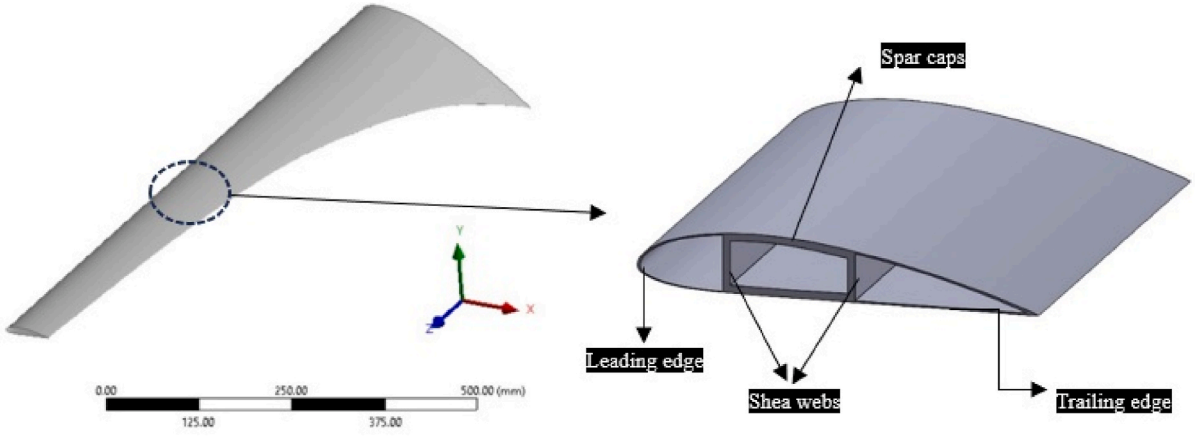

Fig. 6. One meter blade model displaying the cross-sectional area.

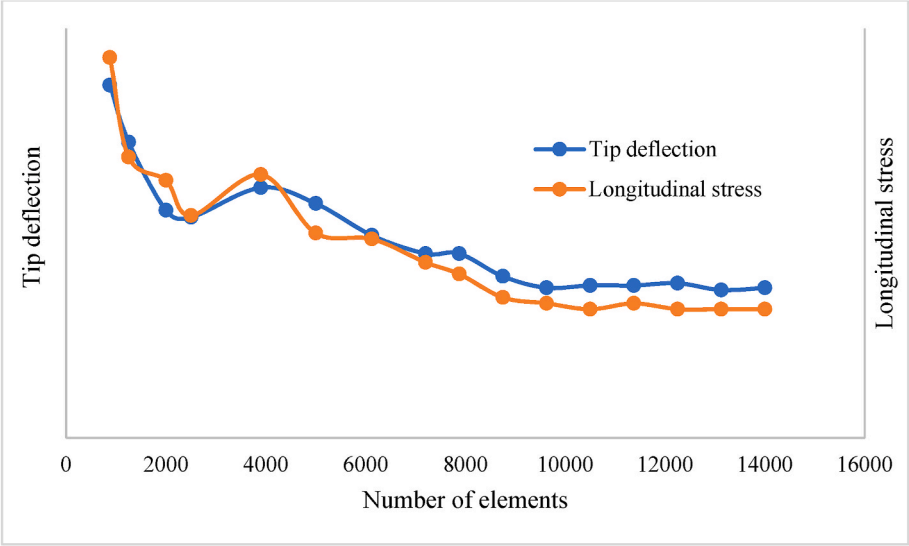

Fig. 7. Convergence based on longitudinal stress and tip deflection.

moment (i.e. edge-wise and flap wise) at the root of the blade are calculated through the BEM code. In the next step, selection of 3D printed materials for the design of the blade is determined by the maximum bending moment. In this study, different 3D printed filament materials of PLA, SGF/PA and SCF/PA are selected as the candidates for small scale design of turbine blades. Because of relatively large bending moment, initially a thick 3D printed material is chosen for the spar caps structure of the blade near the root area. Starting with the maximum thickness in the blade root, the layer numbers in the spar cap sections of the blade decreases until the factor of safety (inverse factor of Tsai-Hill failure index) is fulfilled. Fig. 8 illustrates the thickness distribution along the length of the blade skin on the spar caps. To accommodate the limited number of plies specified for each blade sections along the length, multiple ply drops are introduced along the span-wise blade thickness from the root to the tip.

3. Results and discussions

3.1. Mechanical characterization using experimental mechanics

In this study, 3D printed shear and tension test specimens detailed in section 2.1, Fig. 2 are used to calculate the effective orthotropic properties of RVE and then these properties were used as input data for the FE simulation of 3D printed small scale blade. Representative tensile and shear stress strain curves for each of these tests in conjunction with their corresponding DIC calculated full field strain maps are shown in Figs. 9 and 10 respectively. The Figures captured DIC strain distribution maps illustrating longitudinal strains at the fracture point alongside their corresponding stress-strain curves. Put it simply, the areas of elevated strain in the DIC strain fields coincide with the fracture point evident in the stress-strain curves. Subsequently, elastic constants and strength parameters extracted from these stress-strain curves are listed in Table 7.

It must be noted following the use of ASTM D638, ASTM D5379 and ASTM D2344, the gradient of the linear portion of stress-strain curves in tension and shear were used to calculate the elastic constants of Young's modulus and shear modulus. The ultimate strength in tension and shear were also obtained from the maximum stress values of the curves. Different components of elastic constants and Poisson's ratios (i.e. E_1, E_2, E_3, G_{12}, G_{23}, G_{13}, ν_{13}, ν_{12}, ν_{23}) were also calculated with reference to Fig. 2 and Table 2. In this work, scanning electron microscopy (SEM) was also used to reveal the fracture surface of 3D printed tensile samples (Fig. 11) showing a typical fibre breakage failure mode. In addition, the results of tensile and shear tests on 3D printed specimens made up of PLA investigated in previous works (Gonabadi et al., 2020, 2022b) has been also added into Table 7.

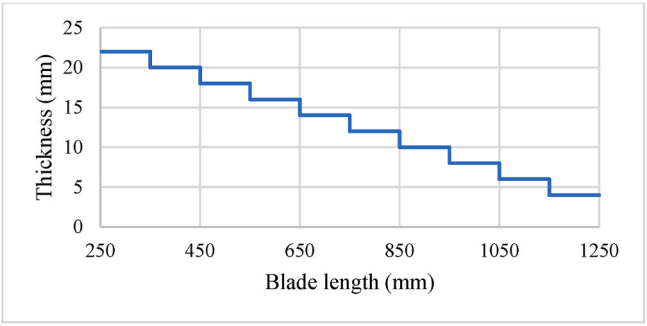

Fig. 8. Distribution of ply drops along the 1-m 3D printed blade length.

3.2. Mechanical characterization using FE micromechanical analysis of RVE

To determine the effective orthotropic characteristics of the RVE, FE stress analysis is also carried out on both micro-scale and meso-scale RVEs in this study. Figs. 12 and 13 depict the FE computed stress fields within the micro and meso-scale RVE models under six different states of uniaxial and shear strains, respectively. Fig. 12 illustrates that stress concentration occurs predominantly around the reinforcing fibres across all loading conditions, suggesting potential failure modes such as interfacial de-bonding between the fibres and matrix interface. Furthermore, the stress fields observed in the meso-scale RVE model (Fig. 13) reveal that under transverse, in-plane shear, and inter-laminar shear loading scenarios (i.e., ε_{33}, γ_{13} and γ_{23}), maximum localized stresses, or stress hot spots, emerge at the intersections of adjacent deposited filaments within overlapping regions. This phenomenon arises due to reduced material volume across these sections and the specific geometric features of the RVE. Consequently, the most vulnerable area within the microstructure lies at these filament intersections, prone to crack initiation and debonding between deposited filaments (inter-layer delamination) during mechanical loading. Moreover, under through-thickness (out-of-plane) and interlaminar shear loading conditions (i.e., ε_{22}, γ_{12} and γ_{23}), the highest localized stresses occur between intra-layer deposited filaments. Such loading regimes can ultimately lead to intra-layer delamination, culminating in the failure of the 3D-printed

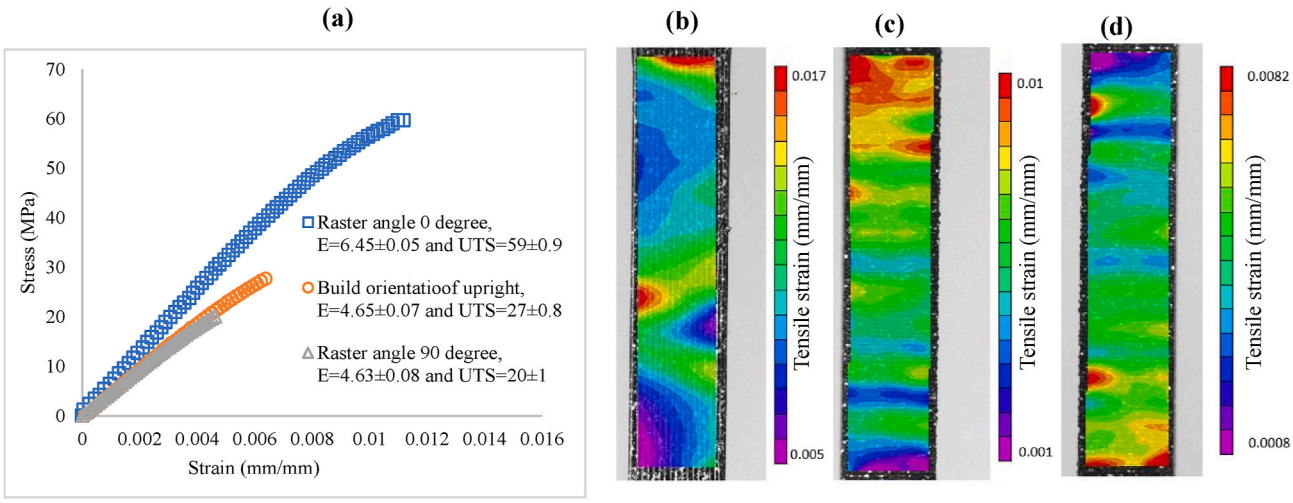

Fig. 9. (a) Tensile stress-strain curves for different build orientation and raster angle of 3D FFF-printed 30% SGF/PA measured by DIC system. DIC strain distribution maps in terms of longitudinal strains prior to the fracture point for 3D FFF-printed tensile specimens of (b), tensile sample with 0° raster angle as depicted in Fig. 2a–(c) tensile sample with the build orientation of upright as shown in Fig. 2b and (d) tensile sample with 90° raster angle as depicted in Fig. 2c. (At least five specimens of each condition were tested and the confidence level for all intervals is 95%).

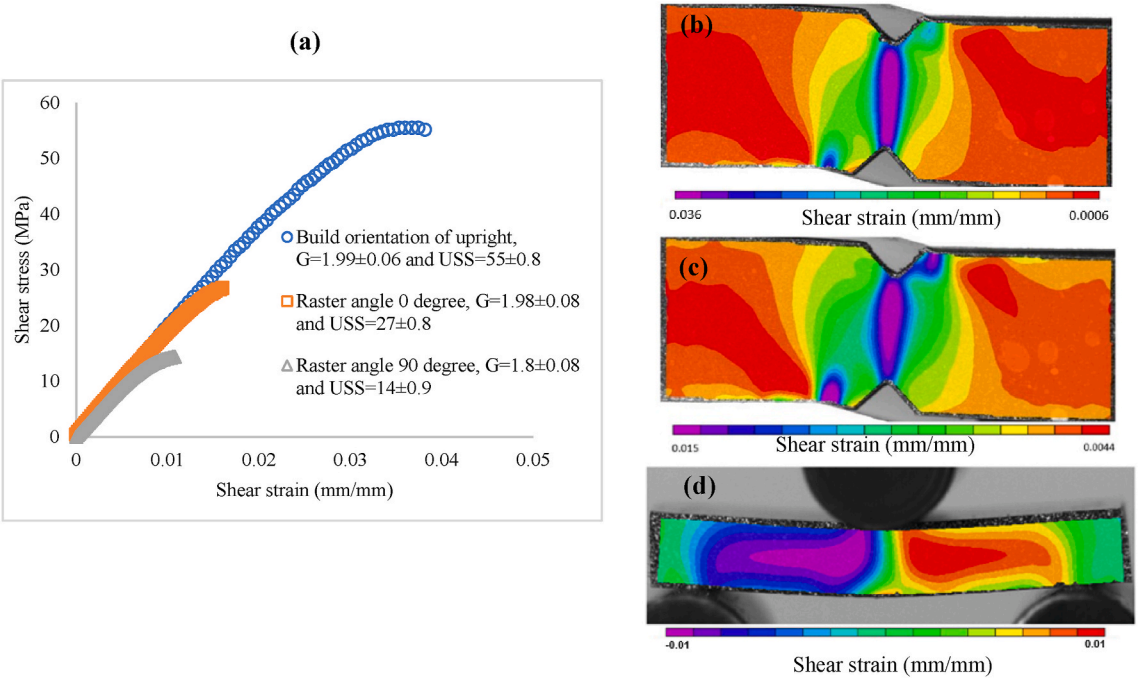

Fig. 10. (a) Shear stress-strain curves for different build orientation and raster angle of 3D FFF-printed 30% SGF/PA measured by DIC system. DIC strain distribution maps in terms of in-plane and inter-laminar shear strains prior to the fracture point for 3D FFF-printed tensile specimens of (b) Iosipescu shear test sample with the build orientation of upright as shown in Fig. 2d–(c) Iosipescu shear test sample with 0° raster angle as shown in Fig. 2f. (d) SBS test sample with 90° raster angle as shown in Fig. 2e. (At least five specimens of each condition were tested and the confidence level for all intervals is 95%).

components. The Finite Element analysis yields effective orthotropic engineering constants of the RVE at the mesoscale levels of RVE, as summarized in Table 8. As can be seen in this Table, the difference between numerically and experimentally calculated orthotropic engineering constants is less than 8% meaning that the mechanical properties obtained by doing shear and tension tests, effectively represent the mechanical properties of mesoscale RVE.

3.2.1. Experimental validation of FE computed mechanical properties through 3 PB test

To further verify the mechanical properties of RVE obtained from the numerical homogenization method, 3D printed rectangular test specimens were manufactured and subjected to Three-Point Bending (3 PB) tests in conjunction with DIC system and the results of load displacement curves and full filed strain maps were compared with FE simulated 3 PB test results. To do this, 3D printed test specimens were manufactured using process parameters detailed in Table 1 at different raster angle and build orientations. Schematic of printing pattern/orientation of 3D printed test specimens is shown in Fig. 14. To construct the FE model of 3D printed test specimens, similar method detailed in previous work (Gonabadi et al., 2022b) were used. During the initial phase of FE modelling for the Three-Point Bending (3 PB) test, a design modelling

Table 7
Orthotropic engineering constants and strength parameters obtained from tensile and shear tests on 3D printed samples. (At least five specimens of each condition were tested and the confidence level for all intervals is 95% based on normal distribution).

Type of test	Properties	30% SGF/PA	15% SCF/PA	PLA
Tension	E_1 (GPa)	6.45 ± 0.05	8.05 ± 0.06	3 ± 0.05
	E_2 (GPa)	4.65 ± 0.07	5.75 ± 0.08	2 ± 0.07
	E_3 (GPa)	4.63 ± 0.08	5.7 ± 0.09	2 ± 0.06
	ν_{12}	0.31 ± 0.02	0.3 ± 0.02	0.29 ± 0.01
	ν_{13}	0.28 ± 0.02	0.29 ± 0.02	0.28 ± 0.01
	ν_{23}	0.24 ± 0.03	0.23 ± 0.03	0.23 ± 0.02
	Longitudinal tensile strength (MPa)	59 ± 0.9	72 ± 0.8	30 ± 1
	Through the thickness tensile strength (MPa)	27 ± 0.8	38 ± 1	19 ± 0.9
	In-plane transverse tensile strength (MPa)	20 ± 1	25 ± 1	10 ± 0.7
Shear	G_{12} (GPa)	1.99 ± 0.06	2.48 ± 0.06	0.91 ± 0.05
	G_{23} (GPa)	1.8 ± 0.08	2.23 ± 0.07	0.8 ± 0.05
	G_{13} (GPa)	1.98 ± 0.08	2.46 ± 0.08	0.9 ± 0.06
	In-plane shear strength (MPa)	55 ± 0.8	64 ±0. 5	30 ± 0.5
	Inter-laminar shear strength (MPa)	27 ±0.8	30 ±0.8	21 ± 0.9
	inter-laminar shear strength (MPa)	14 ± 0.9	18 ± 0.7	17 ± 0.5

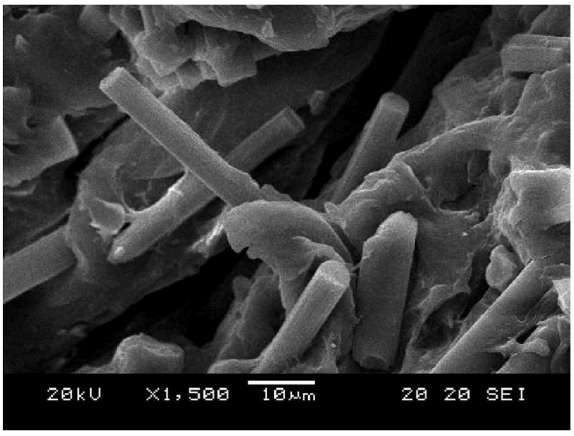

Fig. 11. SEM micrograph showing the fibre breakage in the fracture surface of 3D printed tensile sample.

tool is employed to develop a shell model of the test specimen. This model is structured to replicate the geometry of the specimen utilized in the experiment, adhering to the specifications outlined in ASTM D7264. Utilizing the surface function, a thin surface is generated and subsequently transferred into the ANSYS Composite Processor (ACP) within the FE program, where the orthotropic properties of the meso-scale RVE are defined. DIC and FE computed strain fields for a representative sample (0 ° raster angle) are compared in Fig. 15. Although, altering the build orientation and raster angle leads to varying strain values, the FE and DIC computed strain distribution maps remain unchanged. Therefore, the influence of build orientation and raster angle is shown in Fig. 16 where experimentally and numerically calculated load-displacement curves are compared. The close agreement between FE and experimental results indicates that using homogenization technique to determine the mechanical properties of RVE can predict the performance of actual 3D printed parts with good approximation, this contributes to reducing the necessity for additional experimental repetitions and helps in minimizing manufacturing costs.

3.3. BEM analysis

The Blade Element Momentum model was employed to analyse a 1-m 3D printed tidal turbine blade. Utilizing the input conditions outlined in Table 5, the hydrodynamic model computed the distribution of chord length and twist angle along the blade length for each blade element, as depicted in Fig. 17. Furthermore, Fig. 18 illustrates the calculated distributions of edge-wise (tangential) and flap-wise (axial) forces. At a blade radius of 0.25 m from the rotor centre, the flap-wise bending moment for tidal current velocities of 1 m/s, 2 m/s, and 3 m/s are approximately 220N.m, 890N.m, and 2000 N.m respectively. The flap-wise bending moment increases by a factor of four imposing significant loads on tidal turbine blades when tidal current velocity increases from 1 m/s to 2 m/s. This shows the challenges that designers will encounter when upscaling 3D printed blade for operation in higher tidal current velocities.

3.3.1. FEA of 3D printed blade

It is important to note that all Finite Element (FE) analyses of small-scale blades in this section rely on the distribution of ply drops along the 1-m 3D printed blade length, as illustrated in Fig. 8. In this study, the Tsai-Hill index is used as a failure criterion, although other factors such as tip deflection and maximum strain/stress in the longitudinal direction have been also analysed. Designers find this particularly significant in the context of tidal turbine blades as the blades are also subjected to other sources of loading from waves, turbulence, and shadow effect from the tower which all play crucial roles. In order to locate the hot spots on the 3D printed blade where the risk of potential failure occurs, FE-calculated stress and strain fields, tip deflection, and Tsai-Hill failure criterion for a 3D printed tidal turbine blade made of SCF/PA composite at the tidal current speed of 2 m/s are analysed (Fig. 19). The failure index of 0.455 (safety factor of 2.2) indicates that the 3D printed blade made up of SCF/PA can successfully resist the failure.

Performing ply-by-ply stress analysis enables the prediction of stress distribution throughout the thickness direction of the 3D printed blade, particularly at the hot spot, as illustrated in Fig. 20. The stress distribution gradient across the thickness of the blade reveals that the highest in-plane shear stresses occur at the outer surface, while the greatest inter-laminar shear stresses are observed at the geometric mid-plane. Correspondingly, distribution of Tsai-Hill failure index through the thickness direction shows that potential failure will be induced on the blade surface.

Table 9 shows the results of FE structural analysis of 3D printed SGF/PA, SCF/PA and PLA blades for the tidal current velocities of 2 and 3 m/s. As it can be seen in this Table, the use of PLA material in the blade structure even at the tidal current speed of 2 m/s is not recommended as the inverse failure index (factor of safety) of 0.6 shows high likelihood of failure. As expected from the mechanical properties of RVEs made up of SGF/PA and SCF/PA composite, the Tsai-Hill failure criterion for the 3D printed blade made with SGF/PA composite is bigger than for the SCF/PA blade. At the tidal current speed of 3 m/s, even using the SGF/PA composite blade with a maximum thickness, the FE predicted safety factor is 0.75 suggesting a heightened risk of blade failure. Fig. 21 depicts the correlation between tidal current velocities and both the Tsai-Hill failure index and tip deflection for 3D printed blades composed of SGF/PA and SCF/PA composites. The data indicates that for tidal current velocities exceeding 2.5 m/s, blades constructed with SGF/PA are prone to failure, whereas blades made with SCF/PA can withstand velocities of up to 3 m/s in seawater without experiencing failure. In addition, the relationship between Tsai-Hill failure criterion and tip

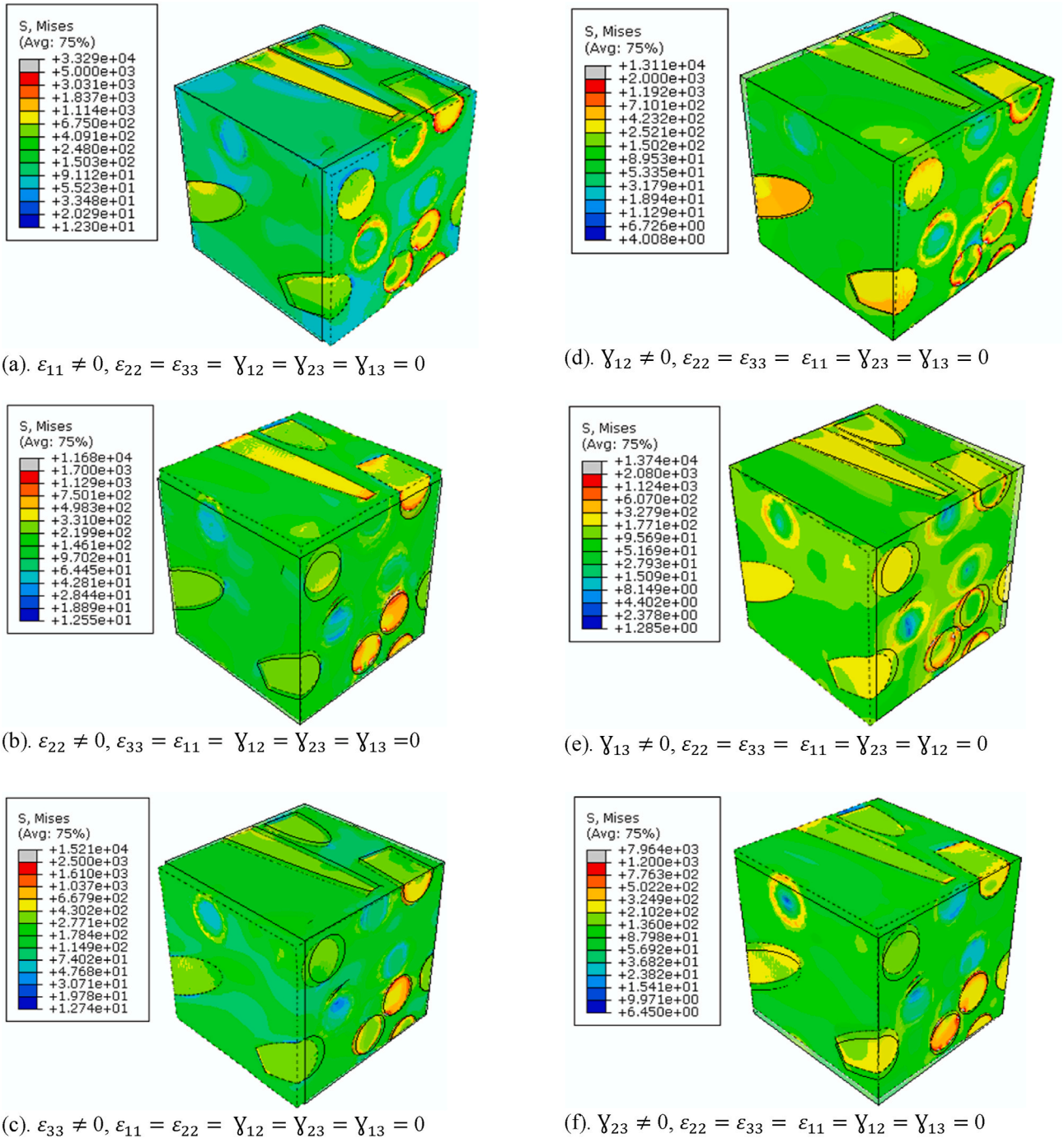

Fig. 12. The stress distributions within the micro-scale model of the RVE of a 3D printed composite part, composed of Short Glass Fiber (SGF) reinforced Polyamide (PA), are analysed under six states of uniaxial and shear strains. The deformed and undeformed shapes of the micro-scale RVE are represented by dashed and solid lines, respectively. It must be noted that the units in this Figure for all RVEs are in Pa.

deflection shows that tip deflection bigger than 13% of blade length is equivalent to the safety factor of 1 meaning high likelihood of blade failure. This can suggest another failure criterion that tidal turbine designers can take into account when using 3D printed technology for the manufacturing process (see Fig. 22).

The thickness variation along the length of the blade skin on the spar caps, as shown in Fig. 8, necessitates the introduction of multiple ply drops along the span-wise blade thickness from the root to the tip, in order to accommodate the specified limited number of plies for each blade section. The use of SCF/PA composite can improve the structural performance of the blade, with a Tsai-Hill failure index roughly 1.3 times lower than SGF/PA for a similar blade design and layer orientation, resulting in a safety factor of 1 for the maximum tidal current velocity of 3 m/s. The superior performance of SCF/PA compared to SGF/PA blades can be attributed to the higher specific stiffness of the former material, albeit at a higher cost. Fig. 20 shows the effect of thickness reduction of the spar structure at the blade root of a 3D printed blade on the safety factor and tip deflection for both SGF/PA and SCF/PA composite materials at the reference tidal current velocity of 2 m/s. For the 3D printed blade made of SGF/PA composite, a slight reduction (10%) in thickness (at the blade root) results in a high likelihood of blade failure (Tsai-Hill failure index factor of 1), while for the SCF/PA 3D printed

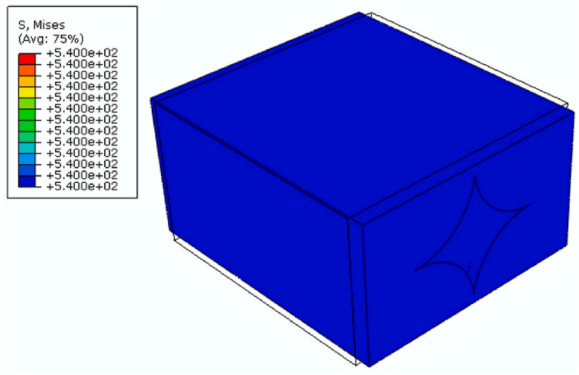

(a). $\varepsilon_{11} \neq 0, \varepsilon_{22} = \varepsilon_{33} = \gamma_{12} = \gamma_{23} = \gamma_{13} = 0$

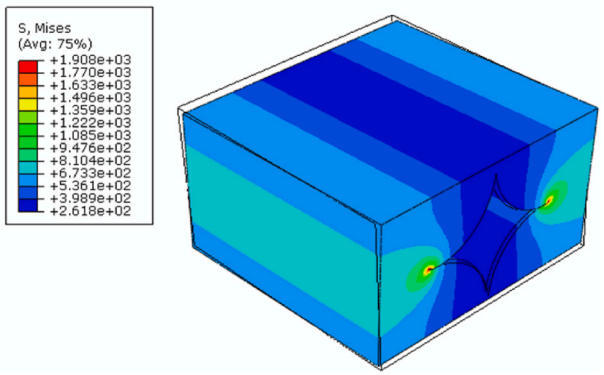

(d). $\gamma_{12} \neq 0, \varepsilon_{22} = \varepsilon_{33} = \varepsilon_{11} = \gamma_{23} = \gamma_{13} = 0$

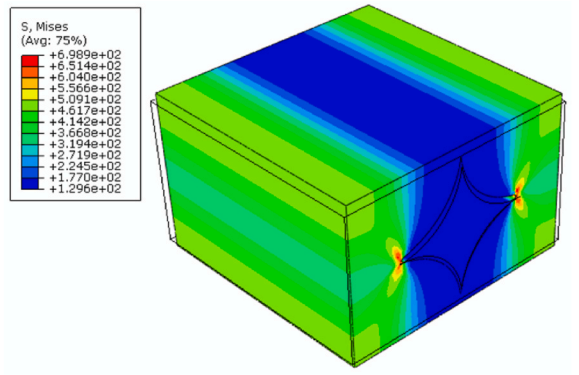

(b). $\varepsilon_{22} \neq 0, \varepsilon_{33} = \varepsilon_{11} = \gamma_{12} = \gamma_{23} = \gamma_{13} = 0$

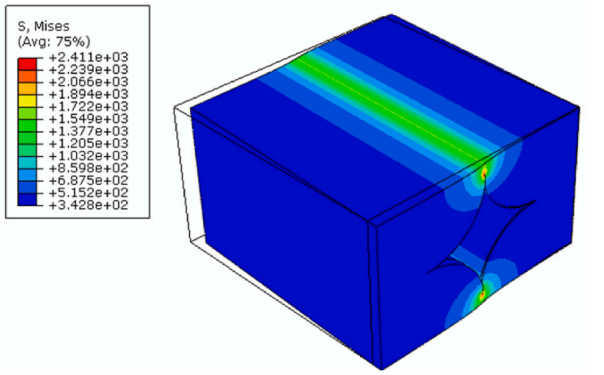

(e). $\gamma_{13} \neq 0, \varepsilon_{22} = \varepsilon_{33} = \varepsilon_{11} = \gamma_{23} = \gamma_{12} = 0$

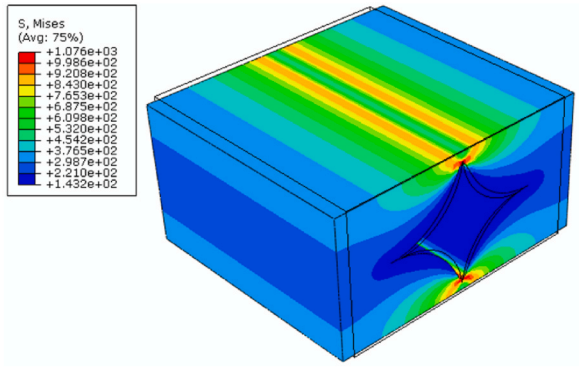

(c). $\varepsilon_{33} \neq 0, \varepsilon_{11} = \varepsilon_{22} = \gamma_{12} = \gamma_{23} = \gamma_{13} = 0$

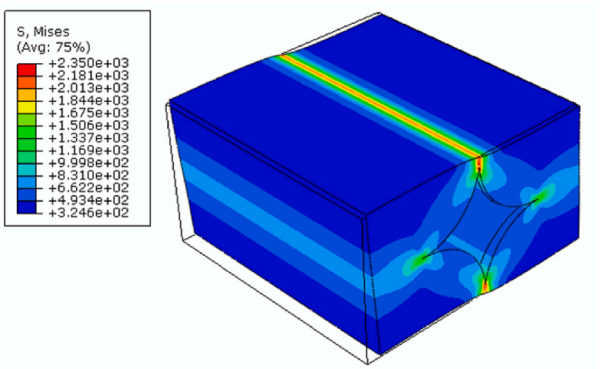

(f). $\gamma_{23} \neq 0, \varepsilon_{22} = \varepsilon_{33} = \varepsilon_{11} = \gamma_{12} = \gamma_{13} = 0$

Fig. 13. The stress distributions within the meso-scale model of the RVE of a 3D printed composite part, fabricated with Short Glass Fiber (SGF) reinforced Polyamide (PA), are examined under six states of uniaxial and shear strains. The deformed and undeformed shapes of the meso-scale RVE are depicted by dashed and solid lines, respectively. It must be noted that the units in this Figure for all RVEs are in Pa.

Table 8
Discrepancies between the components of elastic moduli calculated through FE analysis and those determined experimentally for meso-scale Representative Volume Elements (RVE).

Elements of moduli	E_1 (MPa)	E_2 (MPa)	E_3 (MPa)	ν_{12}	ν_{13}	ν_{23}	G_{12} (MPa)	G_{13} (MPa)	G_{23} (MPa)
SGF/PA (FE)	6765	5027	5044	0.33	0.3	0.26	2154	2154	1938
SCF/PA (FE)	8411	6250	6271	0.32	0.31	0.25	2678	2678	2410
SGF/PA (EXP)	6450	4650	4635	0.31	0.28	0.24	1997	1980	1800
SCF/PA (EXP)	8050	5750	5747	0.3	0.29	0.23	2480	2465	2235
SGF/PA (FE-EXP-Diff)	4.50%	7.50%	8%	6%	6.50%	7.50%	7%	8%	7%
SCF/PA (FE-EXP-Diff)	4%	8%	8%	6%	6.50%	8%	7.40%	7.90%	7.20%

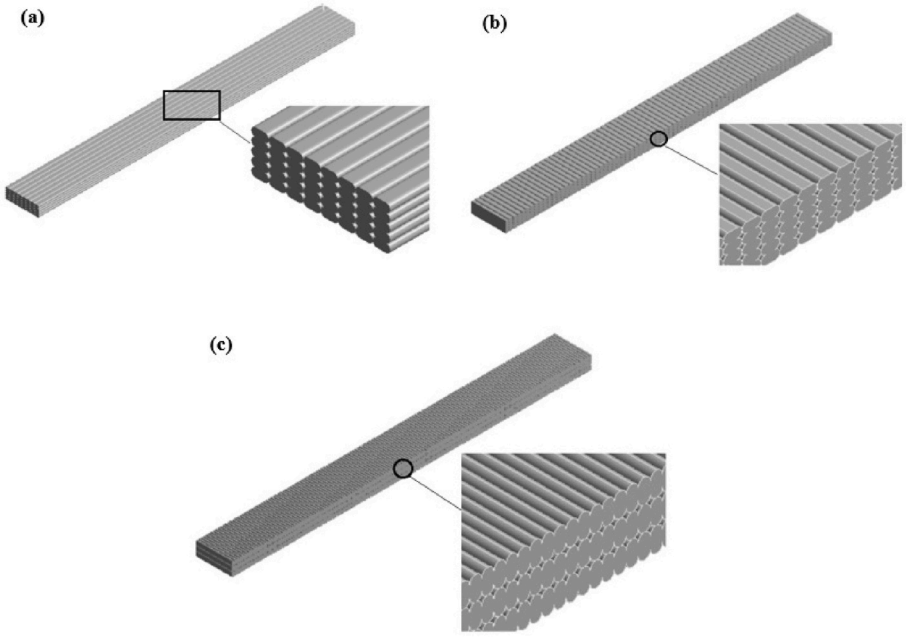

Fig. 14. Schematic representation of SCF/PA 3D printed Three-Point Bending specimens with different raster angle and build orientation. (a) raster angle of 0 °, (b) raster angle of 90 °, (c) build orientation of upright.

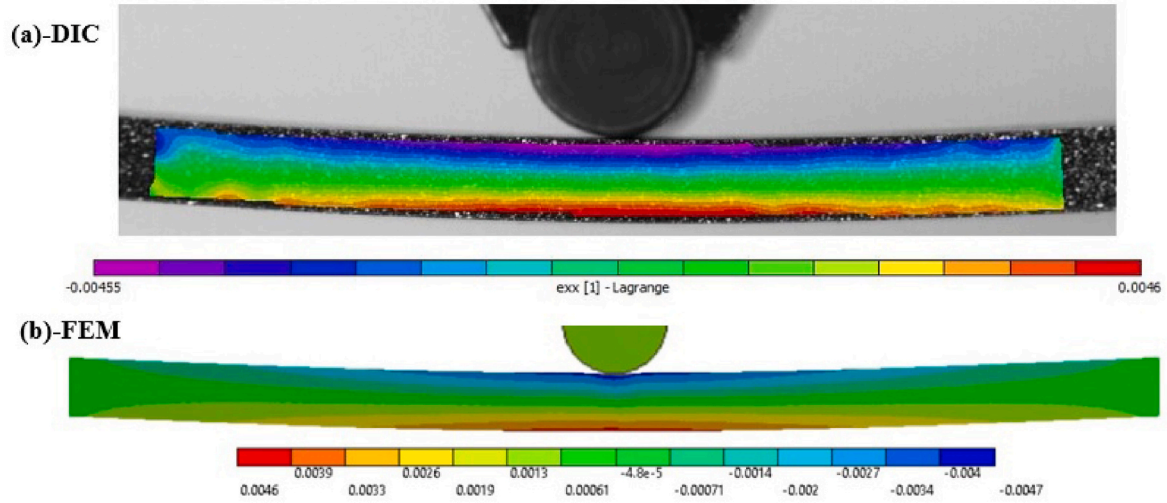

Fig. 15. (a) DIC and (b) FE computed strain distribution maps of SCF/PA 3D printed specimens with 0 ° raster at the maximum deflection of 1.5 mm with the corresponding load of 92 N.

blade, reducing the number of plies by 20% at the root of the blade, the failure index is still satisfactory, suggesting that employing SCF/PA material allows for reducing the weight of the blade by utilizing fewer filament layers, all while maintaining comparable performance to SGF/PA blades. According to the FE model, increasing the laminate thickness of the spar structure in the SGF/PA blade by approximately 15% would yield a safety factor equivalent to that of the SCF/PA blade, assuming identical energy production. However, it is essential to consider that while the SCF/PA blade offers enhanced performance, its higher cost may prompt a cost-benefit analysis, and in some cases, adjusting the size of the blade to address the elevated bending moment at the hot spot for the SGF/PA material might be more cost-effective.

- Analysis of in-plane and interlaminar shear stress through the thickness direction of composite blade skins

As described earlier, conducting a layer-by-layer stress analysis allows for prediction stress distribution across the depth of the 3D printed blade (Fig. 20). The gradient of stress distribution across the blade's thickness demonstrates that the most significant in-plane shear stresses are present on the outer surface, while the most substantial interlaminar shear stresses occur at the geometric midpoint. This is a typical behaviour of composite materials used in the design of tidal turbine blades (Gonabadi et al., 2021b). In fibre-reinforced composite materials like carbon fibre or fiberglass composites, the distribution of interlaminar shear stress across the thickness greatly effects the mechanical behaviour of components such as tidal turbine blades (Gonabadi et al., 2021b). Interlaminar shear stress refers to the stress between adjacent layers of the composite material. This stress varies throughout the thickness in each layer, with the highest stress typically near the mid-plane and decreasing towards the outer surfaces (Ganesan, 2008; Gonabadi et al., 2021c). Factors such as lamina properties, including

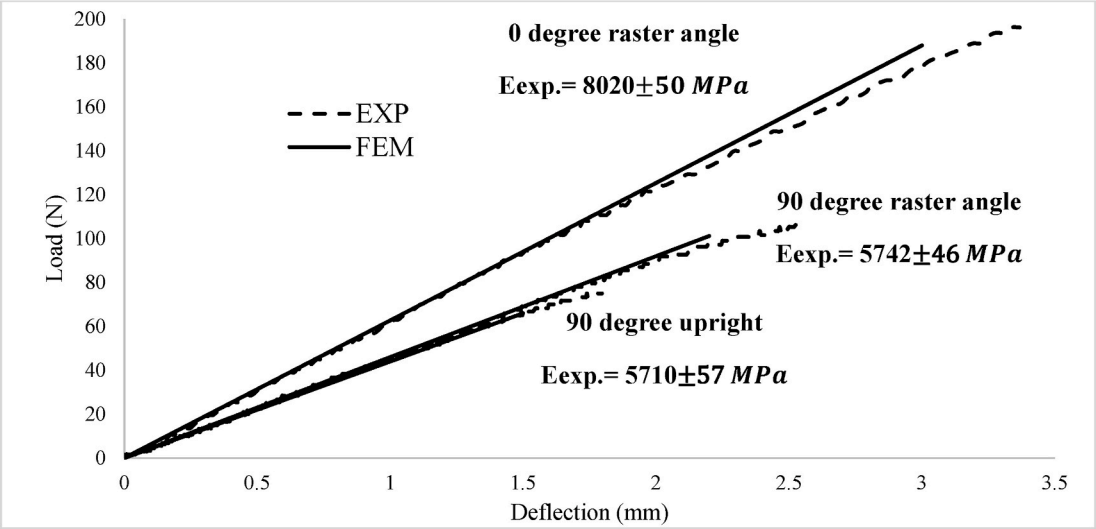

Fig. 16. Experimentally and numerically calculated load-displacement curves within the linear portion obtained from Three-Point Bending tests on SCF/PA 3D printed test specimen. (At least five specimens of each condition were tested and the confidence level for all intervals is 95%).

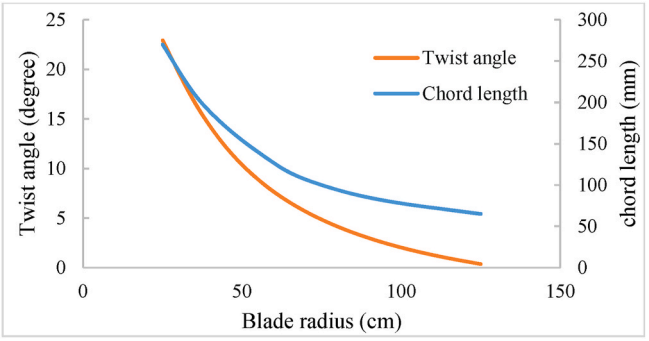

Fig. 17. The variation of twist angle and chord length along the length of the blade.

orientation of deposited filaments significantly impact this distribution, with higher aligned filaments generally experiencing lower shear stresses. Additionally, the interlaminar shear strength, representing the maximum stress before delamination occurs, plays a crucial role, as delamination often initiates in regions experiencing high interlaminar shear stress (McCarthy et al., 2019; Huang et al., 2021).

The distribution of in-plane shear stress within fibre-reinforced composite tidal turbine blades plays a pivotal role in determining their mechanical behaviour (Floreani et al., 2019). This stress, which acts parallel to the laminate's plane, varies across the thickness direction and is affected by factors like loading conditions, stacking sequences of deposited filaments, and material properties (Huang et al., 2021). The distribution of shear stress is intricately linked to lamina stiffness, where higher stiffness laminae, like those with aligned fibres, bear more stress compared to lower stiffness counterparts (Bednarcyk et al., 2007). Additionally, the laminate's resistance to shear deformation is affected by the orientation of reinforcing fibres, impacting the overall stress distribution (Shah et al., 2019). Furthermore, boundary conditions and loading configurations further shape the distribution of in-plane shear stress, with scenarios like bending leading to elevated stress levels near the laminate's outer surfaces and diminish towards the laminate's inner surfaces (Gonabadi et al., 2021c; Nielsen et al., 2017). This non-uniform stress distribution can cause various failure modes such as shear-driven delamination, cracking, and debonding, highlighting the importance of understanding and mitigating these risks to ensure the structural integrity and longevity of composite tidal turbine blades (Izadi Gonabadi, 2019).

4. Validation of FE results against the experimental data

In this study, validation of FE results of 3D printed tidal turbine blade against the experimental data was conducted by comparing the DIC and FE computed strain distribution maps of laboratory scale model of 3D printed blade.

4.1. Fabrication of laboratory scale 3D tidal turbine blade

To manufacture the laboratory-scale 3D printed blade, initially the 3D CAD model of blade was prepared based on the geometry model and dimension shown in Fig. 23. The same composite materials (i.e., 30% SGF/PA and 15% SCF/PA composites) with the 3D printing process parameters detailed in Table 1 were used in Ultimaker Cura program to make the machine code for the FFF 3D printer. The 3D printed laboratory scale blade is shown in Fig. 24. As seen in Fig. 25, the 3D printed blade (200 mm length) was installed into the fixture and at the location past the midpoint of the blade towards the blade tip, quasi-static forces were applied using a flexural testing rig which was designed and manufactured in house. A data logger which was linked with the load cell attached to the flexural testing rig was used to record the variation of load versus displacement on a computer. Additionally, a random black-and-white speckle pattern was applied to the blade. This allowed the DIC system to measure the full-field strain distribution by mapping the surface strain during the load application.

4.2. FE modelling of laboratory scale 3D printed tidal turbine blades

In this study, the ANSYS FE code was utilized to establish a connection between material properties, laboratory-scale tidal turbine blade geometry, and quasi-static loading for structural application assessment. Initially, a 3D shell model of the blade was created using a design modelling tool within ANSYS. This model integrated the radial chord length, twist angle distributions (as depicted in Fig. 23), and hydrofoils from the NACA family. Boundary conditions and loading modes applied to the laboratory-scale blade's FE model mirrored the quasi-static forces experienced during flexural testing (as described in section 4.1). This was achieved using the remote force option in ANSYS. The process of generating the 3D shell model involved creating a 2D sketch for each blade profile using spline functions, followed by generating a thin wall structure between these splined sections using the loft/

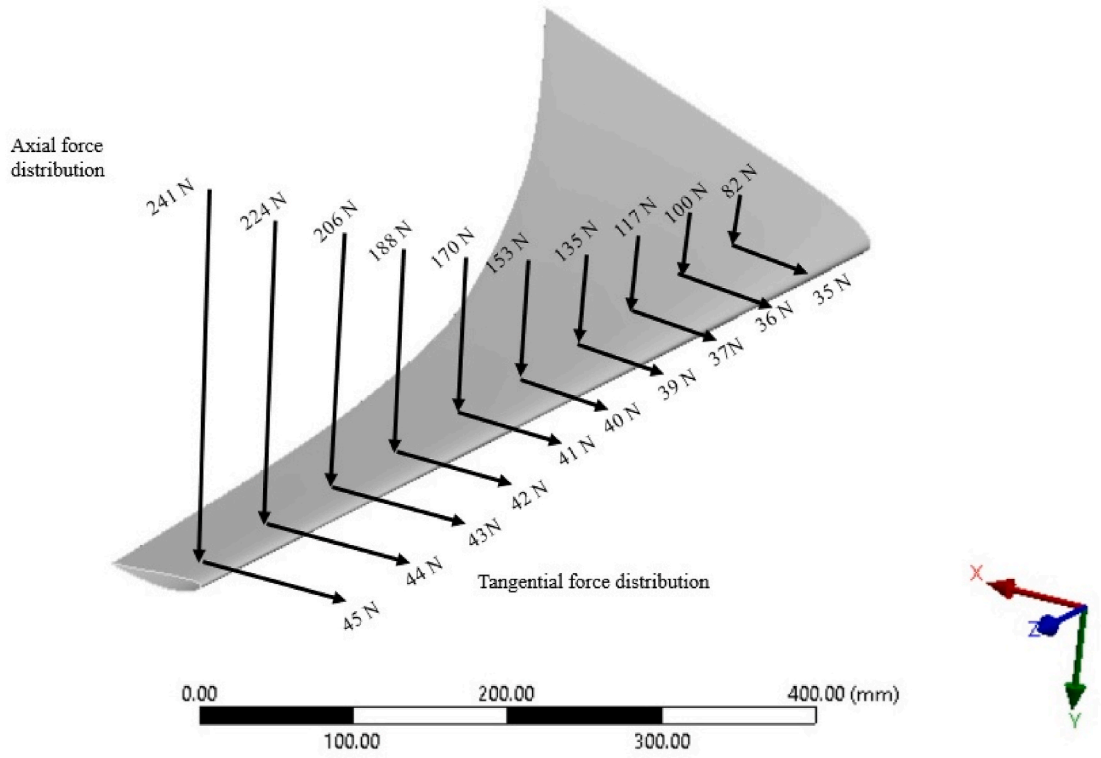

Fig. 18. FE model of 1000 mm 3D printed blade showing the tangential and thrust force distribution calculated from hydrodynamic model at the velocity of 2 m/s tidal current.

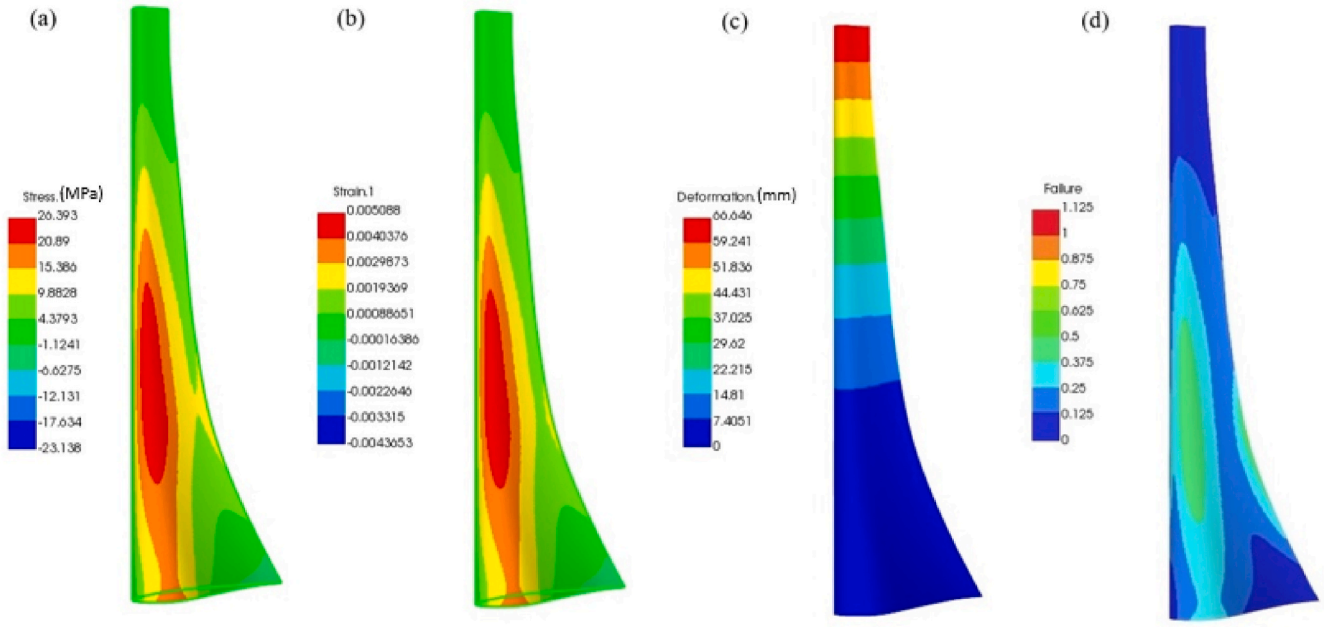

Fig. 19. FE contour plots of SCF/PA 3D printed blade at the tidal current speed of 2 m/s, (a) flap-wise stress, (b) flap-wise strain, (c) tip deflection, (d) Tsai-Hill failure criterion.

skin function. Subsequently, the blade model was imported into the ANSYS Composite Pre-Process module (ACP), where orthotropic engineering constants and strength parameters of the 3D printed materials (specifically RVE with 30% SGF/PA, 15% SCF/PA, and PLA) were incorporated. Finally, the blade was imported into the static structural module of the ANSYS FE program, where boundary conditions (i.e., quasi-static forces) were applied. The FE model of the blade was treated as a cantilever beam, with the root of the blade constrained in all degrees of freedom. It was modelled using linear shell elements (shell 181), each consisting of four nodes with six degrees of freedom at each node (three translations in the x, y, and z directions, and three rotations about the x, y, and z axes). A box spar structure and two shear webs were included in the blade design. To ensure mesh independence and accuracy of FE results, convergence analysis was conducted by refining the mesh density

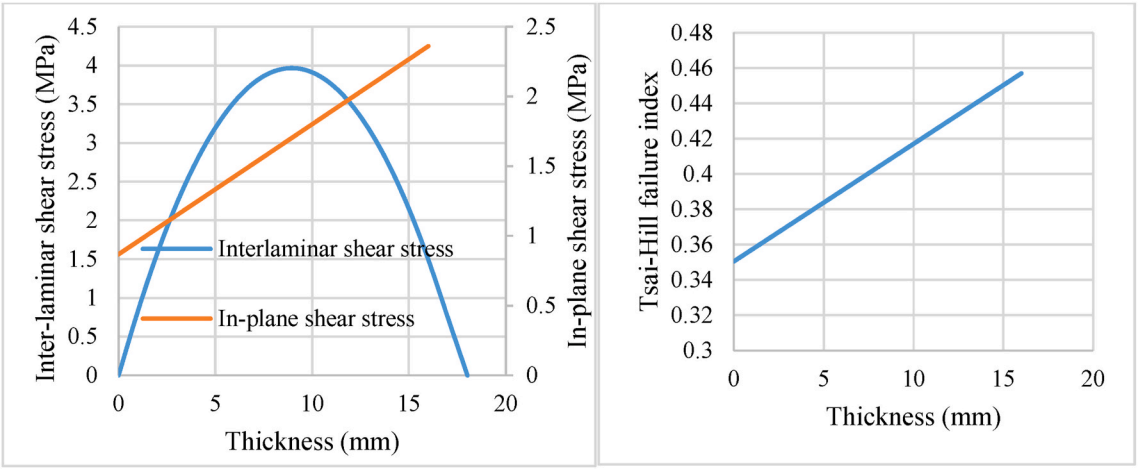

Fig. 20. Predicted (a) distribution of in-plane and inter-laminar shear stresses across the thickness direction and (b) Tsai-Hill failure index at the hot spot of 3D printed made up of SCF/PA composite.

Table 9
Findings from Finite Element (FE) structural analysis of 3D printed blades (1 m in length), conducted at tidal current speeds of 2 and 3 m/s.

	2 m/s			3 m/s		
3D printed materials	**Tip deflection (mm)**	**Flap-wise strain (%)**	**Safety factor (inverse Tsai-Hill failure index)**	**Tip deflection (mm)**	**Flap-wise strain (%)**	**Safety factor (inverse Tsai-Hill failure index)**
SCF/PA composite	66	0.5	2.13	141	1	1
SGF/PA composite	83.5	0.61	1.54	177	1.3	0.75
PLA	187	1.32	0.62	400	2.7	0.29

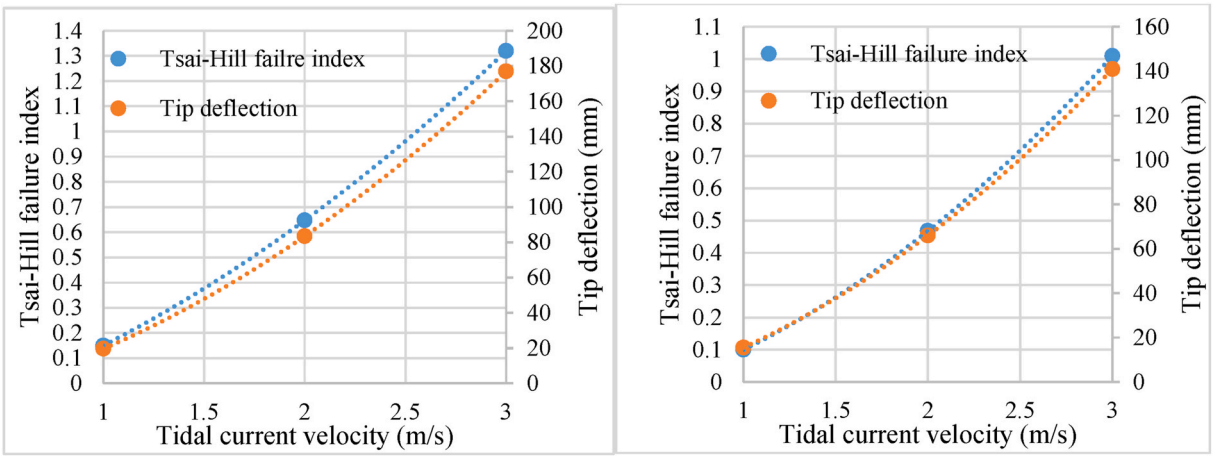

Fig. 21. Variation of Tsai-Hill failure index and tip deflection versus sea water velocity for 3D printed blade made up of (a) SGF/PA composite, (b) SCF/PA composite.

until an appropriate number of elements was determined.

By applying the same boundary condition in flexural testing rig on the FE model of laboratory scale blade, FE computed strain fields in longitudinal direction (i.e. flap-wise strain) were mapped and compared with experimentally (DIC) generated strain fields. As can be seen in Fig. 26, at the displacement of 5 mm there is a good correlation between FE and DIC calculated strain fields and strain The comparison of longitudinal strain along the blade length in both the finite element (FE) model and experimental data (refer to Fig. 27) indicates a strong correlation between the results obtained from experimentation and finite element analysis (FEA). values near the hot spot. Slight difference in terms of strain distribution obtained from FE and DIC is due to the quality of surface condition of 3D printed blade as the surface roughness of actual 3D printed blade was not taken into consideration in the FE modelling. Numerically and experimentally evaluated structural performance of lab-scale 3D printed blade at the displacement of 5 mm is shown in Table 10, showing consistent results. The consistency observed between the numerically and experimentally calculated strain distribution maps (Fig. 26), as well as the corresponding strain values and reaction forces (Table 10) on the laboratory-scale blade, validates the reliability of the Finite Element (FE) investigation presented in this study. Consequently, there is a high level of confidence in utilizing FEM based methodologies to predict the structural integrity of 3D printed small-scale tidal turbine blades.

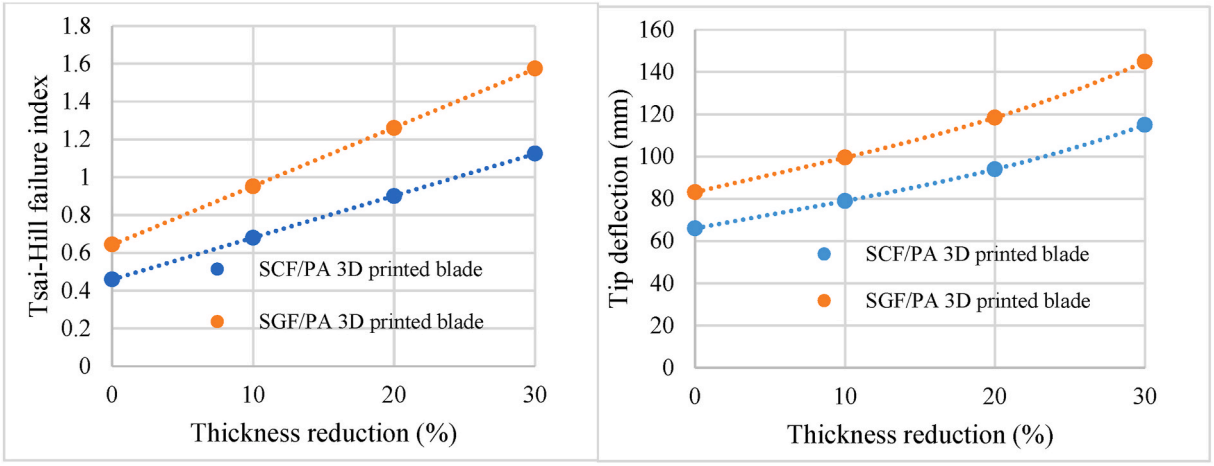

Fig. 22. Predicted effect of thickness reduction of laminate materials (SGF/PA and SCF/PA) of the 3D printed -blade on (a) blade failure and (b) tip deflection in a tidal zone with 2 m/s tidal current velocity.

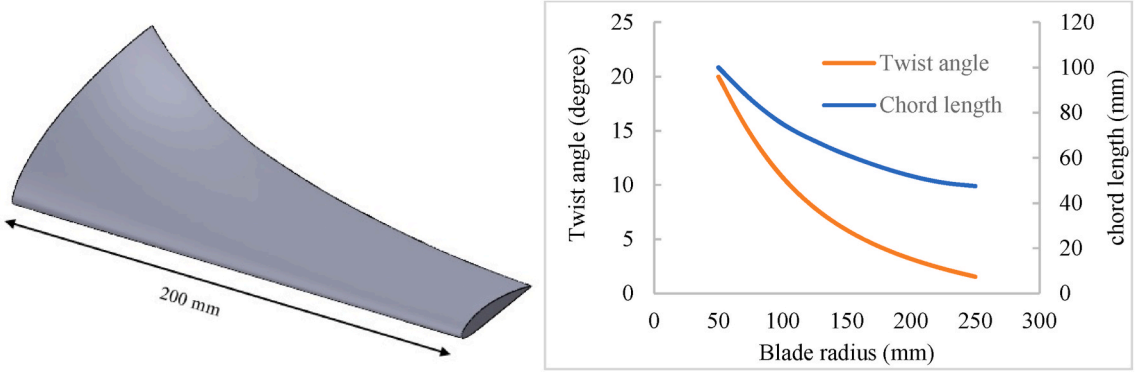

Fig. 23. (a), FE model of 200 mm laboratory scale 3D printed blade and its corresponding (b) distribution of chord length and twist angle along the blade length.

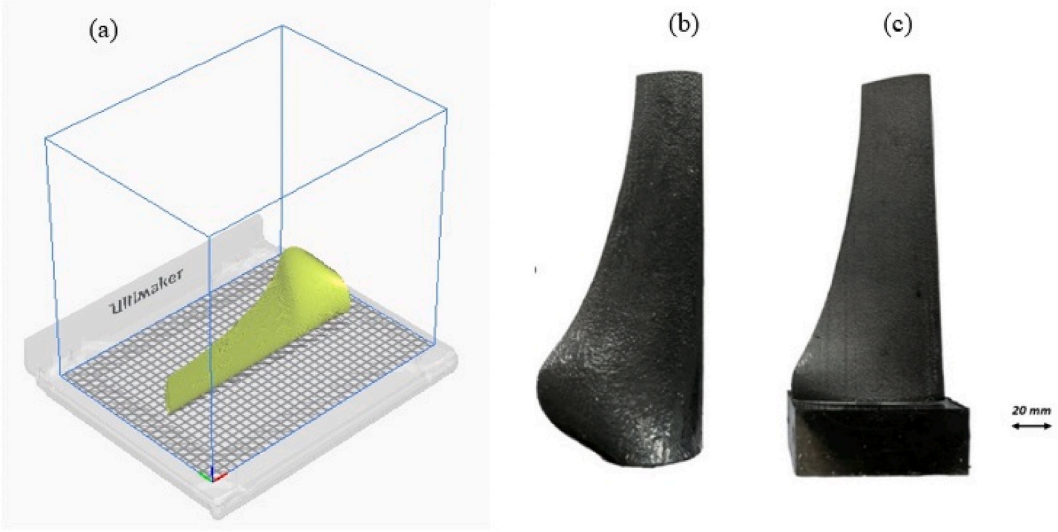

Fig. 24. (a) Machine code model of blade in FFF 3D printer. (b) 3D printed blade, (c), Mounted 3D printed blade in a cube box of cured resin to facilitate fixing in the flexural testing rig.

5. Challenges in using 3D printing technology to manufacture small scale tidal turbine blades

Using additive manufacturing, particularly 3D printing, for constructing small tidal turbine blades offers several benefits, including customization, rapid prototyping, and potential cost reductions. However, there are notable challenges and limitations associated with this approach. Firstly, material selection poses a significant hurdle as not all

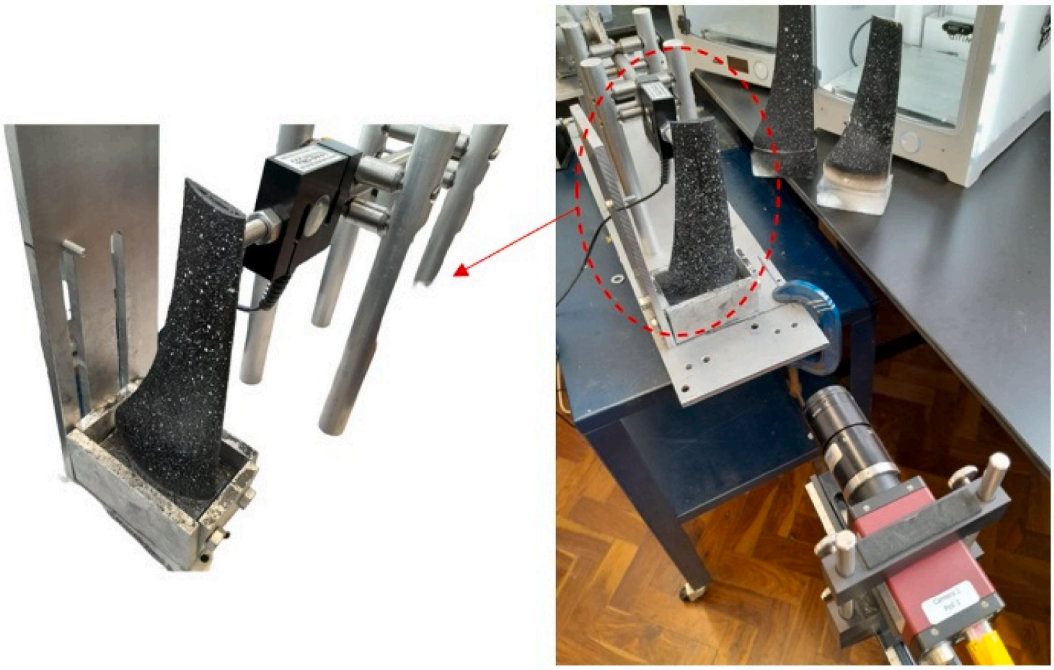

Fig. 25. Flexural testing rig to apply bending load on 3D printed blade.

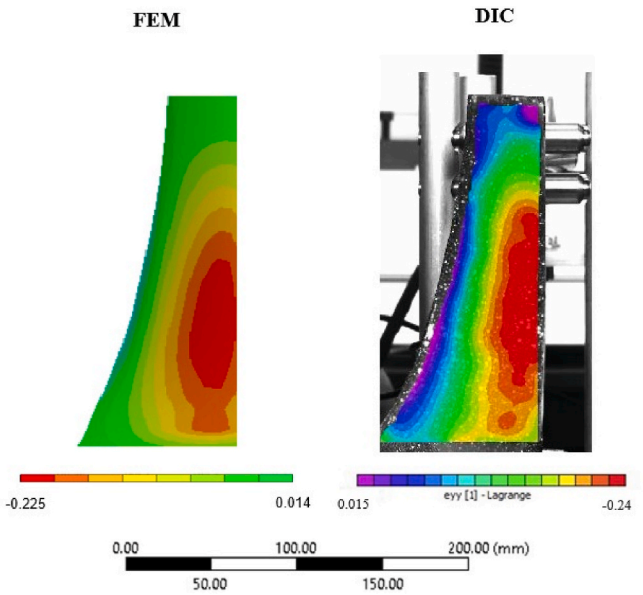

Fig. 26. Numerically (FE) calculated strain fields (i.e. longitudinal strain) against the experimentally (DIC) generated strain fields (flap-wise strain) of SCF/PA 3D printed blade subjected to 50 N bending load.

materials suitable for traditional manufacturing processes may possess the necessary strength, durability, and corrosion resistance required to withstand the harsh marine environment and tidal forces. Furthermore, ensuring adequate durability and fatigue resistance in 3D printed blades necessitates extensive testing, research, and optimization due to the repetitive loading cycles experienced in sea water operation. Surface finish and roughness present additional concerns, as the inherent texture of 3D printed parts may compromise hydrodynamic performance by increasing drag. Post-processing techniques may be required to enhance surface smoothness. Moreover, scaling up production to larger turbine blades poses challenges in terms of size limitations and production time constraints inherent in 3D printing technology. This could deter feasibility and cost-effectiveness compared to traditional manufacturing methods, despite the advantages at smaller scales. Consequently, a multidisciplinary approach is imperative, involving materials science, engineering design, manufacturing processes, and testing methodologies to develop 3D printed tidal turbine blades that meet performance, durability, and cost requirements.

6. Conclusions

This study investigates the possibility of using 3D printing to manufacture small-scale tidal turbine blades. It develops a methodology combining experimental and numerical methods to evaluate structural performance. Mechanical testing and numerical homogenization characterize the blade material's properties. Hydrodynamic analysis establishes boundary conditions, while FE analysis evaluates stress fields and failure probability. Laboratory-scale 3D printing and flexural testing validate FE modelling against experimental data. This study yields several conclusions.

- The close agreement between the FE-computed orthotropic mechanical properties of RVE using homogenization method and the experimentally calculated elements of elastic moduli of RVE using the tensile and shear testing of 3D printed specimens, indicate that FE homogenization technique can be used by the blade designers to measure the effective properties of RVE instead of costly and time consuming experimental procedures of mechanical tests. This can significantly reduce the number of experimental repeats.
- The hydrodynamic analysis emphasized the substantial impact of loadings on 3D printed tidal turbine blades as tidal current velocities escalate from 1 to 3 m/s. This suggests that significant flap-wise bending moments will pose a significant challenge in upscaling turbine designs
- High bending moments experienced during extreme operating conditions, particularly tidal current velocities surpassing 2.5 m/s, are anticipated to induce substantial stresses and tip deformation in 3D printed blades. However, it was observed that the failure index in 3D printed SCF/PA blades under similar loading conditions was lower

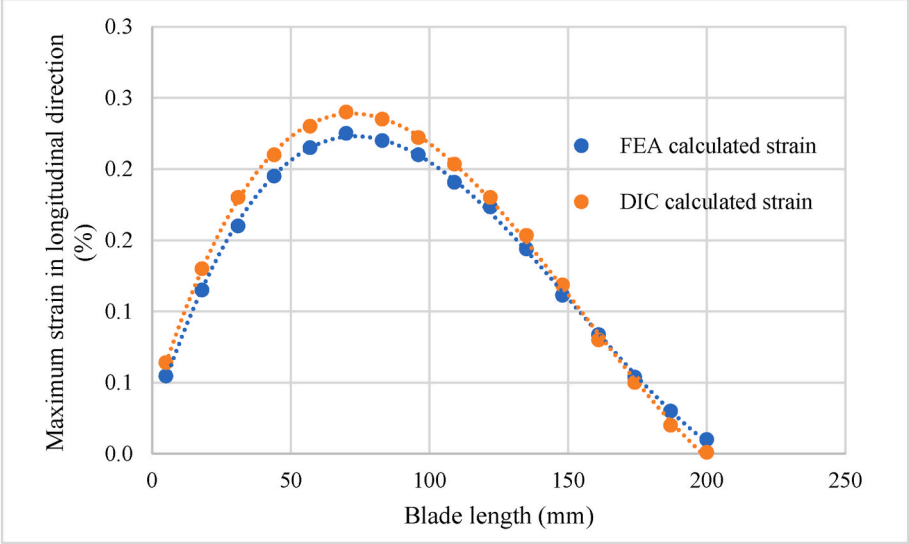

Fig. 27. Comparison of flap-wise strain distribution along the length of the laboratory-scale blade between the finite element (FE) model and experimental data.

Table 10
Structural performance of laboratory scale 3D printed blade (numerical VS experimental) at the tip defection of 5 mm. (At least three lab-scale blade was 3D printed and tested. confidence level for all intervals is 95%).

Lab-scale blade material		FE	EXP
SGF/PA	Reaction force (N)	41	38.2 ± 1.143
	Maximum strain (%)	0.28	0.29 ± 0.02
SCF/PA	Reaction force (N)	53	50.4 ± 1.81
	Maximum strain (%)	0.22	0.236 ± 0.016

compared to 3D printed SGF/PA blades. Specifically, under extreme operating conditions, high flap and edge-wise bending moments led to a safety factor nearing 0.75 (indicative of complete blade failure) for 3D printed SGF/PA blades (1 m in length). Conversely, under the same loading conditions, the safety factor for SCF/PA blades was increased to an acceptable level. Nonetheless, it is worth noting that utilizing SCF/PA material for blade construction would incur higher manufacturing costs. Therefore, it is suggested to employ SGF/PA for fabricating shorter (lower power) tidal turbine blades, as they require less material and entail lower manufacturing costs.

- Incorporating experimental mechanical data for both types of 3D printed materials into the FE model of the blade and considering hydrodynamic loading under representative operating conditions (tidal current velocity of 2 m/s), it is anticipated that SGF/PA blades will require approximately 1.15 times thicker laminates compared to SCF/PA blades to uphold the same safety factor.
- FE analysis of micro and meso-scale RVE serves as a valuable tool for pinpointing localized stresses occurring at the interface between fibres and matrix within the micro-scale model of the RVE. Additionally, it enables the identification of localized stresses at the interfaces between adjacent filaments or layers within the meso-scale model of the RVE. Consequently, this analytical approach allows for the prediction of potential failure modes such as interfacial debonding between fibres and the matrix, inter-layer and intra-layer delamination that may occur in 3D printed tidal turbine blades.
- The efficacy of Finite Element Analysis software as a structural analysis tool for early design iterations has been validated through Digital Image Correlation mapping of the strain field. This is evidenced by the close agreement observed between the strain distribution maps obtained by DIC and FEM, albeit with FEM predicting slightly higher strain values overall. This discrepancy may suggest that the FE model provides conservative criteria in terms of safety factor when utilized as a design tool for 3D printed tidal turbine blades.

The integrated numerical and experimental approach devised in this study, alongside the experimental validation of lab-scale 3D printed blades, showcases the capability to forecast the performance of 3D printed tidal turbine blades across various loading conditions. This methodology offers substantial savings in testing, crucial for evaluating the structural behaviour of tidal turbine blades before industrial deployment, thereby leading to significant cost reductions. Furthermore, the methodology established in this research empowers industrial manufacturers and designers to conduct rapid iterative analyses utilizing Finite Element based mechanical properties of 3D printed materials. This facilitates the selection of additive manufacturing processes by predicting failures and identifying key parameters such as material types, orientations, infill patterns, thickness distributions, and ply drop quantities along the blade length, ultimately enabling the production of high-quality 3D printed tidal turbine blades.

Future works

The future research and development of 3D printed tidal turbine blades requires a focus on addressing existing challenges while maximizing the advantages offered by additive manufacturing technology of 3D printing. Several key areas for future research can been identified as below:

Development of Advanced Materials: Research should continue to explore novel materials with enhanced strength, durability, and resistance to corrosive environment of seawater, specifically tailored for 3D printing processes. This includes investigating composite materials optimized for marine environments.

Fatigue Behaviour: Further investigations are necessary to understand the long-term fatigue behaviour of 3D printed turbine blades under cyclic loading conditions. Extensive fatigue testing in simulated marine environments will be essential to assess performance and identify areas for improvement.

Surface Finish: Research into post-processing techniques and surface treatments is crucial to minimize roughness and improve hydrodynamic efficiency. This may involve exploring new polishing methods, coatings, or additive manufacturing processes capable of producing smoother surface. The quality of surface finish is one of the main limitation in the present study leading to slight difference between the finite element and experimental results.

Scaling up: Overcoming size limitations inherent in 3D printing is crucial for scaling up production to larger turbine blades. Advancements in printing speed, build volume, and process automation are necessary to improve efficiency and cost-effectiveness.

Assessment of lifecycle: Lifecycle assessments are needed to evaluate the environmental impact, energy efficiency, and economic feasibility of 3D printed tidal turbine blades compared to traditional manufacturing methods. Factors such as material sourcing, manufacturing energy consumption, and end-of-life disposal must be considered.

Field testing and Validation: Validation through field testing in tidal environments is essential to verify the performance, reliability, and durability of 3D printed turbine blades. This includes monitoring operational performance, structural integrity, and corrosion resistance over extended period.

CRediT authorship contribution statement

Hassan Gonabadi: Writing – review & editing, Writing – original draft, Validation, Software, Methodology, Investigation, Formal analysis, Conceptualization. **Seyed Farhad Hosseini:** Data curation, Conceptualization. **Yao Chen:** Validation, Data curation. **Steve Bull:** Supervision.

Declaration of competing interest

The authors declare that they have no known competing financial interests or personal relationships that could have appeared to influence the work reported in this paper.

Data availability

No data was used for the research described in the article.

Appendix A. Supplementary data

Supplementary data to this article can be found online at https://doi.org/10.1016/j.oceaneng.2024.118057.

References

Ansys, C., Ansys, C., 2009. User''s Guide Release 12.0. ANSYS Inc.

Arivalagan, S., et al., 2023. Optimization and experimental investigation of 3D printed micro wind turbine blade made of PLA material. Materials 16 (6), 2508.

Astm, P., 2012. *ASTM D5379/D5379M—Standard test Method for Shear Properties of Composite Materials by the V-Notched Beam Method.* West Conshohocken.

Bednarcyk, B.A., Aboudi, J., Yarrington, P.W., 2007. Determination of the Shear Stress Distribution in a Laminate from the Applied Shear Resultant–A Simplified Shear Solution.

Chadha, A., et al., 2019. Effect of fused deposition modelling process parameters on mechanical properties of 3D printed parts. World Journal of Engineering 16 (4), 550–559.

Committee, D., 2008. ASTM D638-08, Standard Test Method for Tensile Properties of Plastics. ASTM International West, Conshohocken, PA, USA.

Davies, P., et al., 2022. Material and structural testing to improve composite tidal turbine blade reliability. International Marine Energy Journal 5 (1), 57–65.

Finnegan, W., et al., 2021. Manufacture of high-performance tidal turbine blades using advanced composite manufacturing technologies. Appl. Compos. Mater. 1–26.

Floreani, C., et al., 2019. Characterization of mode I interlaminar properties of novel composites for tidal turbine blades. In: 13th European Wave and Tidal Energy Conference.

Galvez, G.M., et al., 2022. Finite element analysis of different infill patterns for 3D printed tidal turbine blade. Sustainability 15 (1), 713.

Ganesan, R., 2008. Experimental characterization of interlaminar shear strength. In: Delamination Behaviour of Composites. Elsevier, pp. 117–137.

Glennon, C., et al., 2022. Tidal stream to mainstream: mechanical testing of composite tidal stream blades to de-risk operational design life. Journal of Ocean Engineering and Marine Energy 8 (2), 163–182.

Gonabadi, H., Yadav, A., Bull, S., 2020. The effect of processing parameters on the mechanical characteristics of PLA produced by a 3D FFF printer. Int. J. Adv. Manuf. Technol. 111, 695–709.

Gonabadi, H., et al., 2021a. Investigation of anisotropy effects in glass fibre reinforced polymer composites on tensile and shear properties using full field strain measurement and finite element multi-scale techniques. J. Compos. Mater., 00219983211054232

Gonabadi, H., et al., 2021b. Structural performance of composite tidal turbine blades. Compos. Struct. 278, 114679.

Gonabadi, H., et al., 2021c. Fatigue damage analysis of GFRP composites using digital image correlation. Journal of Ocean Engineering and Marine Energy 7 (1), 25–40.

Gonabadi, H., et al., 2022a. Fatigue life prediction of composite tidal turbine blades. Ocean Eng. 260, 111903.

Gonabadi, H., et al., 2022b. Investigation of the effect of raster angle, build orientation, and infill density on the elastic response of 3D printed parts using finite element microstructural modeling and homogenization techniques. Int. J. Adv. Des. Manuf. Technol. 118 (5), 1485–1510.

Grogan, D.M., et al., 2013. Design of composite tidal turbine blades. Renew. Energy 57, 151–162.

Guessasma, S., 2008. Young's modulus of 2D cellular structures under periodic boundary conditions and subject to structural effects. Comput. Mater. Sci. 44 (2), 552–565.

Harper, P.W., Hallett, S.R., 2015. Advanced numerical modelling techniques for the structural design of composite tidal turbine blades. Ocean Eng. 96, 272–283.

Huang, S., et al., 2021. Characterization of interfacial properties between fibre and polymer matrix in composite materials–A critical review. J. Mater. Res. Technol. 13, 1441–1484.

Izadi Gonabadi, H., 2019. Performance of Low Cost Composites for Tidal Turbine Applications. Newcastle University.

Kamaal, M., et al., 2021. Effect of FDM process parameters on mechanical properties of 3D-printed carbon fibre–PLA composite. Progress in Additive Manufacturing 6, 63–69.

Kennedy, C.R., et al., 2018. Fatigue life of pitch-and stall-regulated composite tidal turbine blades. Renew. Energy 121, 688–699.

Kim, S., 2017. An Integrated Design Approach for Infill Patterning of Fused Deposition Modeling and its Application to an Airfoil. Oak Ridge National Lab.(ORNL), Oak Ridge, TN (United States).

Kim, S., et al., 2018. Graded infill structure of wind turbine blade core accounting for internal stress in big area additive manufacturing. In: Proceedings of the CAMX Composite and Advanced Materials Expo, pp. 15–18. Dallas, TX, USA.

Liu, X., Shapiro, V., 2016. Homogenization of material properties in additively manufactured structures. Comput. Aided Des. 78, 71–82.

Malim, A., et al., 2023. Structural design of a large-scale 3D-printed high-altitude propeller: methodology and experimental validation. Aerospace 10 (3), 256.

Materials, A.C.D.-o.C., 2006. Standard Test Method for Short-Beam Strength of Polymer Matrix Composite Materials and Their Laminates. ASTM International.

McCarthy, E.D., Soutis, C., 2019. Determination of interfacial shear strength in continuous fibre composites by multi-fibre fragmentation: a review. Compos. Appl. Sci. Manuf. 118, 281–292.

Murray, R.E., et al., 2018. Towing tank testing of passively adaptive composite tidal turbine blades and comparison to design tool. Renew. Energy 116, 202–214.

Naveed, N., 2021. Investigate the effects of process parameters on material properties and microstructural changes of 3D-printed specimens using fused deposition modelling (FDM). Mater. Technol. 36 (5), 317–330.

Nielsen, M., et al., 2017. Laminate design for optimised in-plane performance and ease of manufacture. Compos. Struct. 177, 119–128.

Park, S.-I., et al., 2014. Effective mechanical properties of lattice material fabricated by material extrusion additive manufacturing. Addit. Manuf. 1, 12–23.

Porter, K.E., et al., 2020. Flume testing of passively adaptive composite tidal turbine blades under combined wave and current loading. J. Fluid Struct. 93, 102825.

Release, A., 2012. 14.5, *ANSYS Inc*. Canonsburg, USA.

Rouway, M., et al., 2021. 3D printing: rapid manufacturing of a new small-scale tidal turbine blade. Int. J. Adv. Des. Manuf. Technol. 115 (1–2), 61–76.

Shah, S., et al., 2019. Impact resistance and damage tolerance of fiber reinforced composites: a review. Compos. Struct. 217, 100–121.

Spera, D.A., 1994. Wind Turbine Technology.

Sun, C.-T., Vaidya, R.S., 1996. Prediction of composite properties from a representative volume element. Compos. Sci. Technol. 56 (2), 171–179.

Tang, C., et al., 2020. Effect of process parameters on mechanical properties of 3D printed PLA lattice structures. Composites Part C: Open Access 3, 100076.

Tucker III, C.L., Liang, E., 1999. Stiffness predictions for unidirectional short-fiber composites: review and evaluation. Compos. Sci. Technol. 59 (5), 655–671.